

Continuous operation of a coherent 3,000-qubit system

Neng-Chun Chiu^{1,*}, Elias C. Trapp^{1,*}, Jinen Guo^{1,*}, Mohamed H. Abobeih^{1,*}, Luke M. Stewart^{1,*}, Simon Hollerith^{1,*†}, Pavel Stroganov¹, Marcin Kalinowski¹, Alexandra A. Geim¹, Simon J. Evered¹, Sophie H. Li¹, Lisa M. Peters^{1,3}, Dolev Bluvstein¹, Tout T. Wang¹, Markus Greiner¹, Vladan Vuletić², and Mikhail D. Lukin^{1,†}

¹*Department of Physics, Harvard University, Cambridge, MA 02138, USA*

²*Department of Physics and Research Laboratory of Electronics, Massachusetts Institute of Technology, Cambridge, MA 02139, USA*

³*Department of Physics, ETH Zurich, 8093 Zurich, Switzerland*

** These authors contributed equally to this work.*

(Dated: 26th June 2025)

Neutral atoms are a promising platform for quantum science, enabling advances in areas ranging from quantum simulations [1–3] and computation [4–10] to metrology, atomic clocks [11–13] and quantum networking [14–16]. While atom losses typically limit these systems to a pulsed mode, continuous operation [17–20] could significantly enhance cycle rates, remove bottlenecks in metrology [21], and enable deep-circuit quantum evolution through quantum error correction [22, 23]. Here we demonstrate an experimental architecture for high-rate, continuous reloading and operation of a large-scale atom array system while realizing coherent storage and manipulation of quantum information. Our approach utilizes a series of two optical lattice conveyor belts to transport atom reservoirs into the science region, where atoms are repeatedly extracted into optical tweezers without affecting the coherence of qubits stored nearby. Using a reloading rate of 300,000 atoms in tweezers per second, we create over 30,000 initialized qubits per second, which we leverage to assemble and maintain an array of over 3,000 atoms for more than two hours. Furthermore, we demonstrate persistent refilling of the array with atomic qubits in either a spin-polarized or a coherent superposition state while preserving the quantum state of stored qubits. Our results pave the way for realization of large-scale continuously operated atomic clocks, sensors, and fault-tolerant quantum computers.

Neutral atom systems have recently emerged as a leading platform for quantum technologies, enabling advances in quantum simulations [1, 2], quantum computing [4–9], atomic clocks and metrology [11–13], and quantum networking [14–16]. However, an outstanding challenge associated with these systems involves atom loss, originating from errors in entangling operations [4], state-readout [9, 22], and finite trap lifetime [24]. Atom losses necessitate pulsed operation which limits the performance of these quantum systems, including the circuit depth of quantum computation [22, 23], accuracy of atomic clocks [21] and the rate of entanglement generation in quantum networking protocols [25]. For instance in quantum computing, scaling up to large, practical algorithms requires encoding information in logical qubits, protected by repeated quantum error correction (QEC) cycles [26, 27]. While these cycles can suppress error rates far below those of individual physical qubits [26, 27], useful quantum circuits may require billions of operations, which eventually lead to loss of atomic qubits that need to be replenished [9, 22]. Similarly, atomic clock applications would benefit from coherent, continuous operation to improve duty cycles and reduce dead time, thereby enhancing stability and precision by mitigating Dick noise, one of the primary limitations of state-of-the-art optical clocks [21]. Addressing these challenges requires a reliable scheme for fast, continuous reloading of atomic qubits that not only outpaces the rate of errors due to decoherence and loss, but is also consistent with simultaneous coherent qubit storage and manipulation.

[28] and optical clocks [29–31], as well as the realization of continuous Bose-Einstein condensation [32]. While past efforts primarily focused on controlling atomic ensembles, most recently these techniques have been extended to explore continuous reloading with individual atom control [17–20]. If expanded to high reloading rates within a coherence-preserving setting, these pioneering experiments highlight the exciting possibility of fully continuous operation of large-scale atomic systems.

Here, we introduce a tweezer array architecture that enables such coherent continuous operation at large-scale with reloading rates up to 30,000 qubits per second, nearly two orders of magnitude above the current state of the art [18, 19]. Our architecture is based on two serial optical lattice conveyor belts that transport a cloud of laser-cooled ⁸⁷Rb atoms into the field-of-view of our microscope objective (Fig. 1a). From this reservoir cloud, atoms are loaded into optical tweezers “in the dark” (i.e., without laser cooling) and then repeatedly extracted into a “preparation zone”, where they are laser-cooled, imaged, rearranged and initialized into their qubit states. Once initialized, atomic qubits are then transported and iteratively assembled into a large array in the “storage zone”, where dynamical decoupling is applied to maintain qubit coherence. Qubits in the storage zone are spatially protected against scattered cooling light by avoiding direct line-of-sight to the magneto-optical trap (MOT), and spectrally protected by light-shifting the cooling transition out of resonance (“shielding”) [33]. We demonstrate continuous atom replenishment and maintenance of more than 3,000 storage array atoms for more than two hours,

Recent experiments have enabled continuous atomic

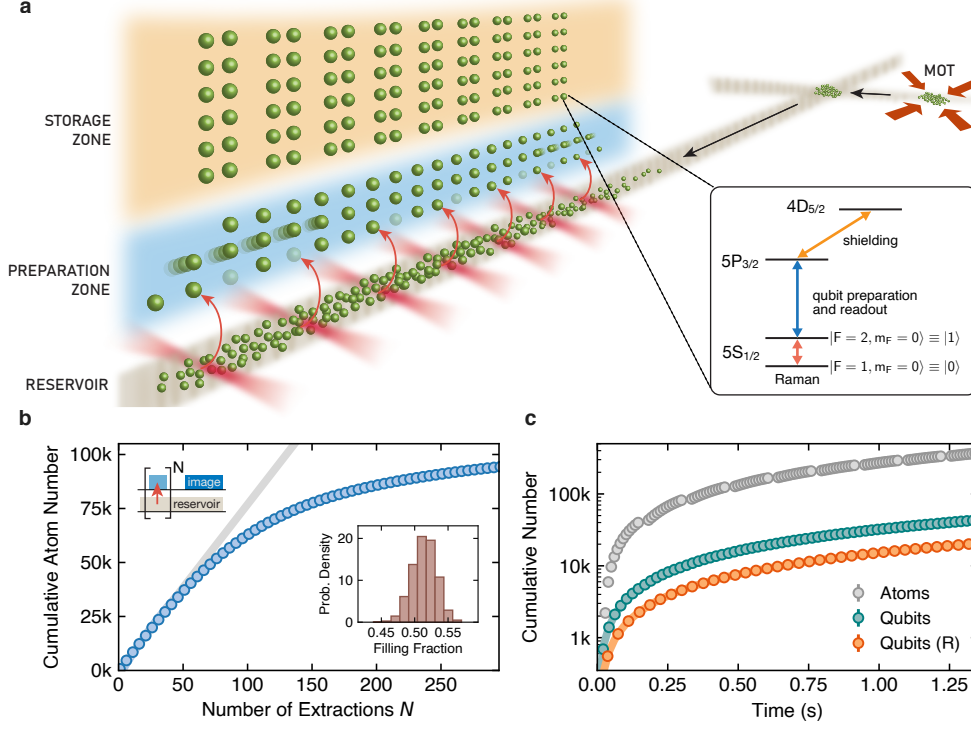


Figure 1. Atom array architecture for continuous reloading. **a**, A cloud of laser-cooled atoms is transported over 0.5m from a separate MOT region into the science region via two optical lattice conveyor belts crossed at an angle. In the science region, the optical lattice serves as an atomic reservoir, from which a 2D array of optical tweezers repeatedly extracts atoms into the “preparation zone”. Here, atoms are laser-cooled, rearranged into a defect-free array, and their qubit state initialized, then transferred into a large-scale storage tweezer array. Our dual-lattice scheme avoids direct line-of-sight between the tweezer arrays and MOT location, and enables fully concurrent preparation and replenishment of the atomic reservoir. Inset: Relevant atomic levels of ^{87}Rb . During qubit preparation, storage qubits are protected from near-resonant photon scattering with the $5S_{1/2} \rightarrow 5P_{3/2}$ transition by light-shifting the excited state (“shielding”). Single-qubit gates are implemented via optical Raman transitions that drive clock states $|0\rangle$ and $|1\rangle$ (Methods). **b**, Cumulative number of atoms obtained by N -repeated tweezer extractions from a single lattice reservoir (see schematic), where we observe a decline in tweezer filling fraction after ~ 70 repeated extractions due to reservoir depletion. For reference, the gray line indicates 50% array filling. Inset: Histogram of tweezer filling fractions for the first 30 extractions from the reservoir. Notably, no laser cooling is applied during the tweezer loading process. **c**, Cumulative number of atoms/qubits obtained by tweezer extraction from repeatedly replaced lattice reservoirs. The gray markers indicate an atom flux of $\sim 300,000$ atoms/s after light-assisted collisions, where the brief interruptions originate from the second transport stage of reservoir replacement during which no reservoir is present. Performing the qubit preparation sequence after each extraction, we achieve a continuous *qubit* flux of 15,000 qubits/s with rearrangement (orange) and 30,000 qubits/s without rearrangement (green).

well-beyond the trap lifetime of about 60 s (Fig. 2c). Furthermore, we sustain the storage zone with either spin-polarized qubits (Z -basis) or qubits in the equal superposition state (X -basis) for, in principle, unlimited duration (Fig. 4b,c).

CONTINUOUS RELOADING FROM A LATTICE RESERVOIR

Our dual-lattice architecture is designed for uninterrupted high-rate qubit reloading that enables repetitive usage and periodic replacement of an atomic reservoir. The experiment starts by loading around 4 million ^{87}Rb atoms from a MOT into an optical lattice con-

veyor belt [34–37]. Then, the atom cloud is transported through a differential pumping tube to the separate science chamber, where it is transferred to a second lattice conveyor belt and delivered into the microscope field-of-view to serve as an atomic reservoir (see ED Fig. 1 and ED Fig. 3). Using this two-stage procedure, a fresh reservoir of 2.5 million 120 μK cold atoms arrives in the science region every 150 ms. From the lattice reservoir, atoms are repeatedly loaded into a dynamic optical tweezer array of 120×12 sites, generated by a pair of crossed acousto-optic deflectors (AODs). To load atoms, we switch on AOD tweezers overlapped with the lattice reservoir and immediately transport captured atoms into the preparation zone region placed 220 μm above. This procedure takes less than 2 ms and, importantly, allows for multiple

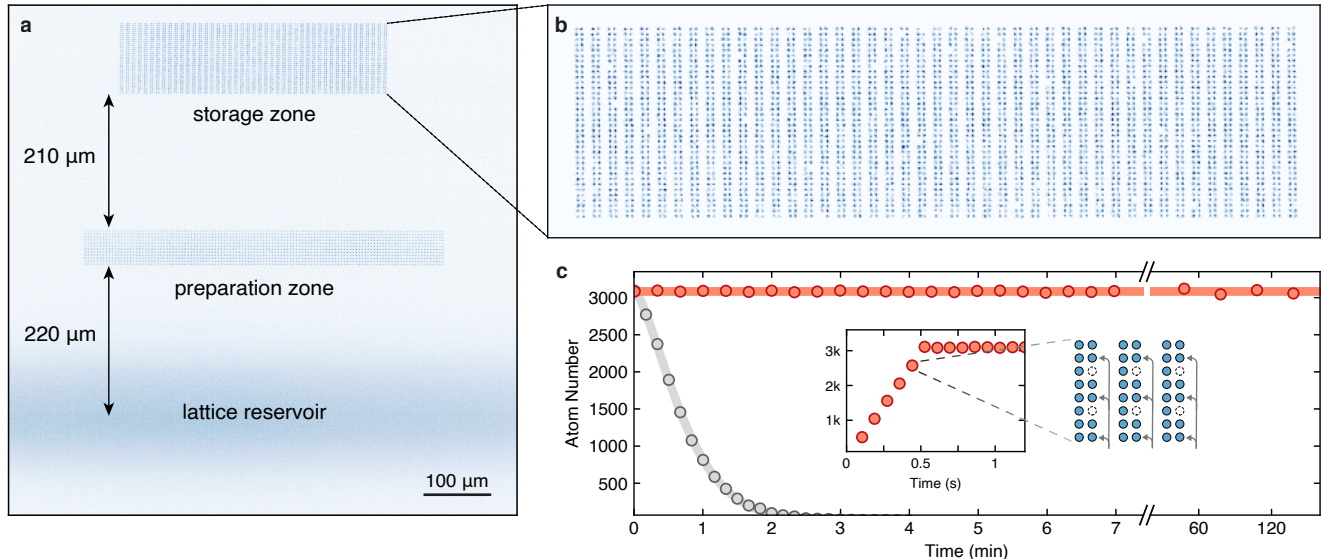


Figure 2. **Iterative assembly and continuous maintenance of a large-scale atomic array.** **a**, Atom fluorescence image outlining the zone architecture consisting of lattice reservoir, 1,440-site preparation zone, and 3,240-site storage zone. (Averaged) images of each zone are exposed separately and combined with different weights for visualization purposes. **b**, Single-shot fluorescence image of 3,217 atoms in the 3,240-site storage array (99.3% filling). **c**, Iterative construction and continuous maintenance of a large-scale atomic array. Initial assembly occurs in ≈ 0.5 s via six loading iterations (inset). Afterward, one of six segments (“subarrays”) is ejected from the storage array and refilled with a fresh set of atoms every ~ 80 ms (see also ED Fig. 6 and Supplementary Movie). Here, we show cyclic subarray replenishment and continuous maintenance of a 3,000+ atomic array for over 2 hours of operation, far beyond the tweezer-limited lifetime of ~ 60 s (gray). At the final datapoint, $t = 2.3$ h, over 50 million individually imaged and rearranged atoms have been cycled through the storage array.

extraction cycles from a single reservoir. Following the extraction, atoms in AOD tweezers are transferred to a static tweezer array generated by a spatial light modulator (SLM).

Fig. 1b demonstrates the results of repeated tweezer extraction from a single lattice reservoir. Here, we extract atoms for multiple cycles and only image and count single atoms after the final extraction cycle, and quote the cumulative number by summing the atom counts over all N cycles. We find that, initially, array filling fractions of $> 50\%$ are comparable to conventional tweezer loading from a MOT [38], but gradually decline as the reservoir is depleted (see also ED Fig. 4). A key aspect of our dual-lattice design is the ability to extract atoms from one reservoir while preparing and delivering a fresh reservoir to the science chamber. By replacing reservoirs as they are depleted, this approach overcomes capacity limits of any single reservoir. In Fig. 1c, we demonstrate this by repeatedly extracting atoms into the preparation zone as before, now replacing the reservoir every 60 tweezer loading cycles. As a result, we achieve a flux of $\sim 300,000$ atoms in tweezers per second, corresponding to the maximum rate at which reservoir atoms can be extracted.

Notably, in contrast to the conventional approach to tweezer loading [38], no laser cooling is applied during the extraction process. We attribute the ability to load optical tweezers “in the dark” to a combination

of stochastic overlap with atoms in the reservoir, and atomic collisions similar to the notion of a dimple trap [39] (Methods). While previous experiments [17–19] have relied on dissipative laser cooling or tweezer-lattice intensity ramps when loading fresh atoms from the reservoir, our scattering-free method helps preserve coherence of nearby storage qubits and avoiding lattice ramp-down enables repetitive usage of the reservoir.

In order to prepare atomic qubits, we perform an initialization procedure after every extraction from the reservoir (see ED Fig. 5). Each step of this procedure relies on two counter-propagating laser beams local to the preparation zone and aligned coaxially with an externally applied static magnetic field (Methods) [22]. First, an explicit parity-projection pulse via finite-field polarization gradient cooling (PGC) on a red-detuned $F = 2 \rightarrow F' = 3$ transition prevents multiply-occupied optical tweezers. We continue laser cooling via PGC during AOD-to-SLM handover, then apply a resonant pushout pulse to eliminate atoms in out-of-plane traps [10]. This is followed by high-contrast, inherently background-free imaging (Methods). Afterward, we arrange atoms into a defect-free array while further laser cooling via electromagnetically induced transparency (EIT) with light blue-detuned from the $F = 2 \rightarrow F' = 2$ transition [40]. Finally, atoms are initialized to the qubit state $|0\rangle$ by optical pumping on the $F = 1 \rightarrow F' = 0$ transition, res-

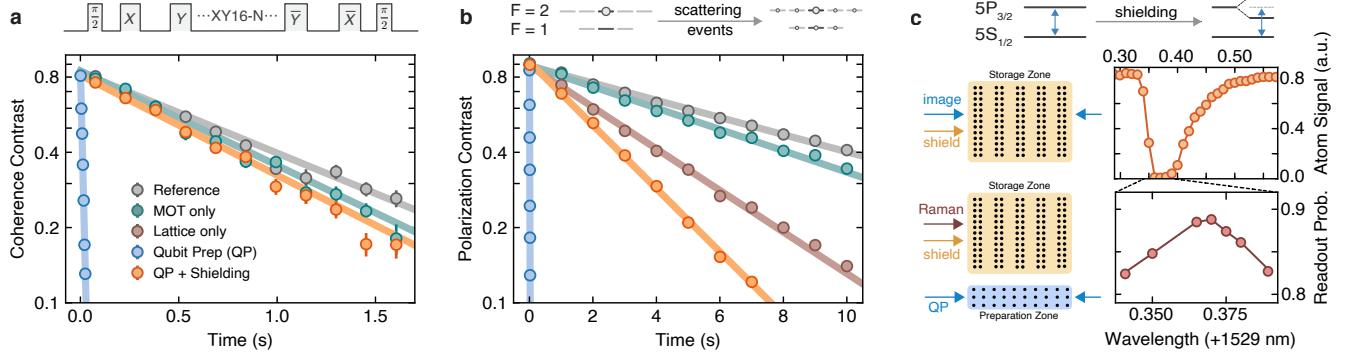


Figure 3. **Benchmarking concurrent qubit preparation.** **a**, Coherence contrast under various conditions when applying N -repetitions of an XY16 dynamical decoupling (DD) sequence with π -pulse spacing $2\tau \approx 1.6$ ms to storage qubits, where the reference measurement yields $T_2 = 1.34(4)$ s (gray). Operating the distant MOT in parallel to DD, we observe a minimal effect on coherence (green) compared to the reference, but a strong effect when additionally imaging in the preparation zone (blue). By applying qubit shielding, we restore coherence almost fully (orange, $T_2 = 1.09(3)$ s). **b**, A similar comparison probing depolarization of qubits initialized in $|1\rangle$ with the reference measurement $T_1 = 12.6(1)$ s (gray). While operating the MOT simultaneously has insignificant effect on storage qubits (green), additionally imaging in the preparation zone results in rapid qubit depolarization (blue). Similar to before, this can be mitigated by shielding storage qubits from near-resonant light (orange, $T_1 = 3.43(3)$ s), mainly limited by off-resonant Raman scattering from the lattice light to which the shielding is ineffective (brown). A similar investigation for $|0\rangle$ state depolarization along with all measured T_1 - and T_2 -times is presented in ED Fig. 8. For subfigures (a-b), the difference of qubit populations measured in $|0\rangle$ and $|1\rangle$ provides the contrast (Methods). **c**, Shielding light spectroscopy on storage qubits. First, we image the storage array while applying low-power shielding light at variable wavelength to resolve the $4D_{5/2}$ resonance by suppression of imaging signal (top). In a fine-scan, we optimize for storage qubit coherence under DD while imaging in the preparation zone by maximizing the readout probability in $|0\rangle$ (bottom).

ulting in a state preparation and measurement (SPAM) fidelity of $\sim 98\%$ within $20 \mu\text{s}$. Under optimal conditions and without atom sorting, the qubit preparation sequence takes 20 ms (Methods).

Fig. 1c shows the result of repeatedly extracting atoms and performing the qubit preparation sequence as described above, while the lattice reservoir is replaced in parallel every few tweezer extraction cycles. As a result, we achieve a *qubit flux* of over 30,000 qubits per second when choosing to not rearrange atoms. With atom sorting, the qubit preparation time approximately doubles and we obtain up to 15,000 qubits per second, rearranged into defect-free batches of 600 qubits. In all cases, the qubit preparation time exceeds the time required for the second transport stage of reservoir replacement; as such, there is always a reservoir present for tweezer extraction and the qubit flux is uninterrupted.

ITERATIVE ASSEMBLY AND MAINTENANCE OF A LARGE ATOM ARRAY

After the preparation sequence, the rearranged array is transported to the storage zone which consists of $3,240$ (90×36) SLM-generated optical tweezers with an average trap depth of $270 \mu\text{K}$. The storage tweezer array features alternating regularly-spaced columns for lossless atom transport in between (Methods), and is positioned with sufficient distance to the preparation zone and the lattice reservoir to limit crosstalk between zones (Fig. 2a).

We assemble the storage array in six iterations, each time transferring atoms into one of six segments (“subarrays”) interspersed throughout the storage array (Methods). Preparation and loading of each subarray, including atom transport to the storage zone, takes roughly 80 ms (mostly limited by rearrangement time and image data transfer). Assembly of the entire storage array is completed in ≈ 500 ms with an averaged loading of 3,193 atoms (98.5% filling fraction) over 300 trials. Fig. 2b shows a single-shot fluorescence image of 3,217 atoms loaded into the array.

In Fig. 2c, we demonstrate the ability to maintain over 3,000 atoms in the storage array for over two hours of continuous operation. After initial storage array assembly, we sequentially eject and refill the longest-stored subarray with a concurrently prepared set of fresh atoms from the preparation zone (see Supplementary Movie). In parallel to atom preparation and subsequent replenishment, we replace the lattice reservoir every other tweezer extraction cycle without affecting the storage zone array. Using these techniques, we replenish atoms on much faster timescales than their tweezer-limited lifetime, and therefore enable operation that is, in principle, indefinite.

COHERENCE DURING CONTINUOUS OPERATION

The ability to reload qubits while preserving coherence of existing qubits is essential for applications in deep-

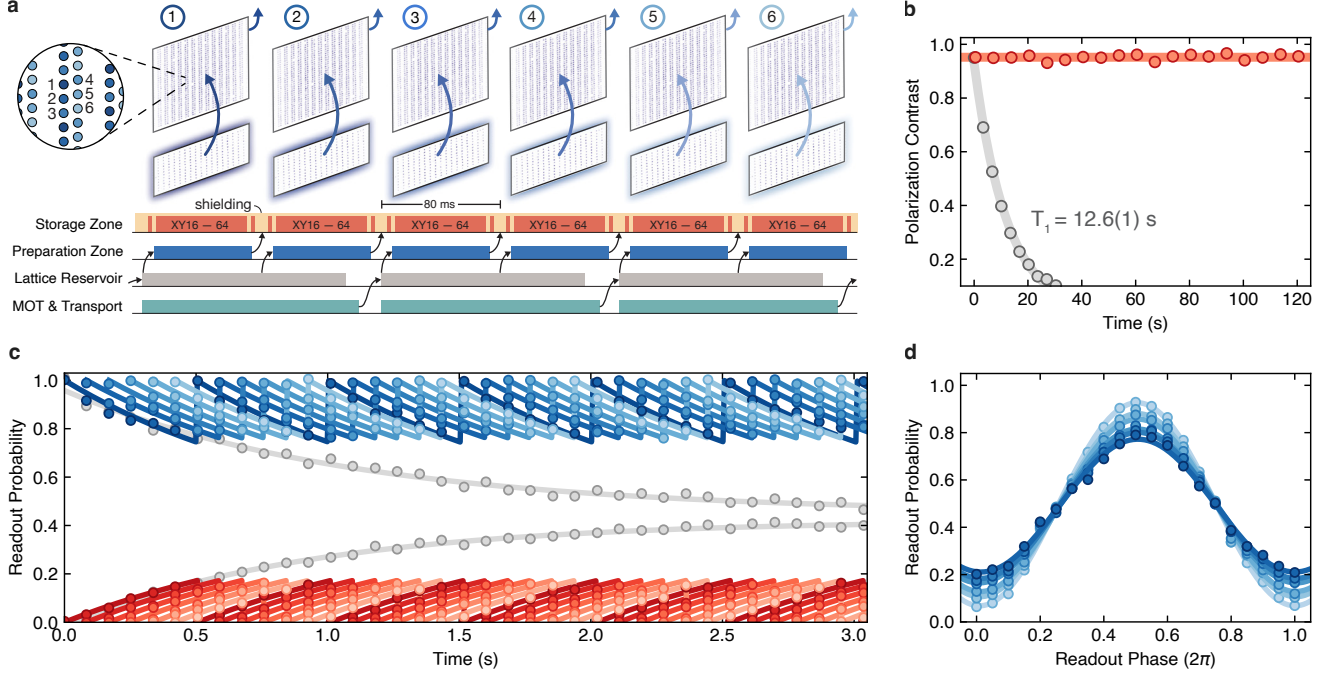


Figure 4. **Continuous reloading while maintaining storage qubit coherence.** **a**, Time sequence visualizing our continuous reloading protocol (see also ED Fig. 9 and Supplementary Movie). Following the initial storage array assembly, the longest-stored subarray is ejected and refilled with a preloaded set of qubits from the preparation zone every ~ 80 ms, while storage zone shielding is applied throughout. For subfigures (c-d), storage qubits are placed in the equal superposition state and undergo an XY16-64 decoupling sequence during each reloading cycle. **b**, Continuously reloading storage zone qubits, we maintain a high degree of storage array polarization (red) for, in principle, unbounded duration. For reference, we provide a T_1 measurement without qubit replenishment (gray). **c**, Similar to (b), now additionally applying an $X_{\pi/2} - (\text{XY16-64}) - X_{-\pi/2}$ dynamical decoupling sequence during each subarray replenishment. We probe coherence of each subarray at various times during the replenishment cycle by reading out qubits in state $|0\rangle$ (blue) or $|1\rangle$ (red) as detailed in Methods. Individual subarrays (color shading) are unaffected by adjacent qubit reloading, and their dephasing is offset in time due to the cyclic subarray reloading protocol. The exponential sawtooth overlays are guides to the eye. For reference, we provide the T_2 measurement of a single subarray under the same cyclic decoupling sequence without qubit replenishment (gray). **d**, After multiple rounds of reloading under dynamical decoupling, we apply a final $\pi/2$ -pulse to read out in different qubit bases. Complementary to (c), the observed coherence contrast varies for each subarray (color shading) due to the time-offset in subarray replenishment.

circuit quantum computation and high-bandwidth metrology [22, 32, 41]. To address this challenge, in Fig. 3a we first investigate the impact of a simultaneously operating MOT on storage qubit coherence. We observe a coherence time of $T_2 = 1.15(3)$ s when applying dynamical decoupling in the presence of the distant MOT, which shows minor modification compared to a reference measurement without the MOT ($T_2 = 1.34(4)$ s). In Fig. 3b, we find a similar result when probing storage qubit polarization via T_1 measurements with and without the MOT. Therefore, by preventing a direct line-of-sight between MOT and qubits, our angled dual-lattice transport scheme successfully disentangles the scattering-intense initial capture of an atomic gas from parallel quantum operations [30, 42].

In addition to the MOT, the coherence of existing qubits can be affected by scattered light and magnetic

field changes during mid-circuit qubit preparation. To mitigate this, our beam architecture operates under constant finite magnetic field [22] and is localized to the preparation zone. However, we initially observe in Fig. 3a that storage qubit coherence is strongly affected by beam crosstalk during the preparation zone imaging procedure. To suppress this effect, we protect qubits from near-resonant scattering by light-shifting the excited state [33] as shown in Fig. 3c, and find that the coherence time can be nearly completely restored ($T_2 = 1.09(3)$ s). Additionally, we probe storage qubit depolarization under the same conditions in Fig. 3b, resulting in a similar conclusion. Here, however, one observes an increased T_1 -decay compared to a reference measurement despite shielding, which is largely dominated by off-resonant scattering from the lattice light. This increase does not measurably affect our T_2 , but can be further mitigated by, for ex-

ample, greater reservoir distance from the storage array, smaller lattice reservoir waist, or larger lattice detuning.

Building on these results, we now assess atom loss replenishment in simple quantum circuits by continuously replacing storage zone qubits while maintaining coherence. In Fig. 4b, we first demonstrate continuous reloading and maintenance of a large array of spin-polarized storage qubits. Similar to Fig. 2c, we now repeatedly prepare freshly initialized *qubit* subarrays in the preparation zone, then eject and refill the oldest subarray in the storage zone as shown schematically in Fig. 4a (see also ED Fig. 9). Continuously replenishing qubits allows us to sustain a high degree of storage array polarization for, in principle, unbounded duration; here, we show maintenance of over 3,000 qubits for two minutes.

Finally, in Figs. 4c,d we demonstrate the ability to reload and sustain a large array of atomic qubits in a coherent superposition state. While shielding and replenishing qubits as in Fig. 4b, we additionally rotate storage qubits into state $|+\rangle$ and sustain coherence by applying a dynamical decoupling sequence during each subarray reloading cycle. Shortly before replenishing a qubit subarray with fresh qubits from the preparation zone, we map coherence into population by rotating all storage qubits into state $|0\rangle$, eject and replace the oldest qubits with newly spin-polarized ones, then rotate back into state $|+\rangle$ as a new reloading cycle starts. This enables us to keep qubits in a superposition state at about 90% duty cycle, while the coherence of individual subarrays remains unaffected by concurrent reloading cycles.

DISCUSSION AND OUTLOOK

Our experiments demonstrate a new atom array architecture that enables continuous operation with reloading rates of up to 30,000 initialized qubits per second while preserving coherence across a rearranged large-scale qubit array. The results can be extended along several directions. First, the qubit preparation time can be significantly shortened through optimized readout and the use of FPGA-based and/or AI-optimized rearrangement protocols [43, 44]. Second, larger preparation zone arrays can be engineered by fully utilizing the system's optical field-of-view. We estimate that these technical improvements would lead to a more than five-fold increase in qubit reloading rate, as this rate is directly proportional to qubit preparation time and preparation zone size. In addition, while the present experiments demonstrate continuous operation for over two hours, achieving much longer operation would benefit from active stabilization of the SLM-AOD overlap or automated beam alignment procedures. Finally, higher-power trapping lasers and high-efficiency diffractive optics, such as metasurfaces [45], can be immediately deployed to scale the storage and preparation zone size, supporting continuous operation of tens of thousands of atomic qubits.

Our results open up a range of new scientific opportuni-

ties based on atom array platforms. In particular, our method is directly compatible with a zoned architecture for quantum computation involving Rydberg-mediated entangling gates, local optical Raman control, and dynamically reconfigurable qubit arrays [9, 22]. This architecture therefore presents a promising approach towards the implementation of deep, fault-tolerant quantum circuits using error correction. In a complementary experiment conducted in a separate apparatus, we demonstrate the core components of such a fault-tolerant quantum processor, including a method for mid-circuit loss-resolving qubit readout and re-use as well as deep-circuit protocols involving logical qubit teleportation, below-threshold repeated error correction, and universal fault-tolerant processing [22]. Atom losses play a major role in these experiments [23], and the ultimate circuit depth is directly limited by atomic reservoir depletion.

Taken together, our experiments open the door for realizing large-scale error-corrected quantum processors. For example, accounting for the current entangling gate fidelity ($\sim 99.5\%$) and atom loss rate, at a 1 ms duration per gate layer we estimate that 15,000 rearranged qubits per second should be sufficient to replenish lost atoms in a quantum processor with about 10,000 physical qubits. Furthermore, realistic improvements in entangling gate fidelities to $\sim 99.9\%$ and reloading flux to 80,000 qubits per second could enable the operation of several hundred surface code logical qubits with a logical failure rate down to 10^{-8} [46]. Moreover, the natural compatibility of this architecture with high-rate quantum low-density parity check (LDPC) codes will likely unlock further improvement in quantum processor performance [47, 48].

Beyond applications in quantum computation, a continuously operating atom array system could overcome several limitations in quantum metrology [21], enabling high-bandwidth and entanglement-enhanced precision quantum sensing [12, 13]. Furthermore, a continuous stream of atomic qubits is essential to achieve fast generation of remote entanglement in quantum networking applications [14, 15, 25]. Finally, our high-rate reloading scheme and the transition from pulsed to continuous operation that it enables may be utilized to improve the performance of a broad class of cold-atom experiments, including quantum simulation, sensing and precision measurements.

Note added. During the finalization of this manuscript, we became aware of related works demonstrating coherence preservation during atom replenishment [49, 50].

ACKNOWLEDGMENTS

We thank Yicheng Bao, Sergio Cantu, Jean Dalibard, Sepehr Ebadi, Manuel Endres, Tilman Esslinger, Brandon Grinkemeyer, Niki Jepsen, Shimon Kolkowitz, Alexander Lukin, Tom Manovitz, John Robinson, Pedro Sales Rodriguez, Giulia Semeghini, Jun Ye, Johannes Zeiher and Harry Zhou for insightful discus-

sions, and Nicholas Lyu for programming the backend of our experimental control system. We also thank Sebastian Geier, Jim MacArthur and Tzu-Ken Shen for help on the experiment. We acknowledge financial support from the US Department of Energy (DOE Quantum Systems Accelerator Center, contract number 7568717), IARPA and the Army Research Office, under the Entangled Logical Qubits program (Cooperative Agreement Number W911NF-23-2-0219), DARPA ONISQ program (grant number W911NF2010021) and MeasQuIT program (grant number HR0011-24-9-0359), the Center for Ultracold Atoms (an NSF Physics Frontier Center), the National Science Foundation (grant numbers PHY-2012023 and CCF-2313084) and QuEra Computing. M.H.A. acknowledges support by a Rubicon Grant from the Netherlands Organization for Scientific Research (NWO). S.H. acknowledges funding through the Harvard Quantum Initiative Postdoctoral Fellowship in Quantum Science and Engineering. S.J.E. acknowledges support from the National Defense Science and Engineer-

ing Graduate (NDSEG) fellowship. D.B. acknowledges support from the Fannie and John Hertz Foundation.

Author contributions: N.C.C., E.C.T., S.H., J.G., L.M.S., M.H.A., T.T.W. planned the experiments, performed measurements, analyzed the data, and contributed to building the experimental apparatus. P.S. and M.K. contributed to the experimental control system. A.A.G., S.J.E., S.H.L. and D.B. contributed to development of methods and techniques for continuous operation. L.M.P. contributed to data interpretation. All work was supervised by M.G., V.V. and M.D.L. All authors discussed the results and contributed to the manuscript.

Corresponding author: Correspondence should be addressed to Simon Hollerith (shollerith@fas.harvard.edu) and Mikhail D. Lukin (lukin@physics.harvard.edu).

Competing interests: M.G., V.V., and M.D.L. are co-founders and shareholders, V.V. is Chief Technology Officer, and M.D.L. is Chief Scientist of QuEra Computing.

-
- [1] A. Browaeys and T. Lahaye, Many-body physics with individually controlled Rydberg atoms, *Nature Physics* **16**, 132 (2020).
 - [2] C. Gross and I. Bloch, Quantum simulations with ultracold atoms in optical lattices, *Science* **357**, 995 (2017).
 - [3] Xu, M. *et al.*, A neutral-atom Hubbard quantum simulator in the cryogenic regime, *Nature* (2025).
 - [4] Evered, S. J. *et al.*, High-fidelity parallel entangling gates on a neutral-atom quantum computer, *Nature* **622**, 268 (2023).
 - [5] Muniz, J. A. *et al.*, High-Fidelity Universal Gates in the ^{171}Yb Ground-State Nuclear-Spin Qubit, *PRX Quantum* **6**, 020334 (2025).
 - [6] R. B.-S. Tsai, X. Sun, A. L. Shaw, R. Finkelstein, and M. Endres, Benchmarking and Fidelity Response Theory of High-Fidelity Rydberg Entangling Gates, *PRX Quantum* **6**, 010331 (2025).
 - [7] Peper, M. *et al.*, Spectroscopy and Modeling of ^{171}Yb Rydberg States for High-Fidelity Two-Qubit Gates, *Phys. Rev. X* **15**, 011009 (2025).
 - [8] Radnaev, A. G. *et al.*, A universal neutral-atom quantum computer with individual optical addressing and non-destructive readout, *arXiv* (2025), 2408.08288 [quant-ph].
 - [9] Bluvstein, D. *et al.*, Logical quantum processor based on reconfigurable atom arrays, *Nature* **626**, 58 (2024).
 - [10] Manetsch, H. J. *et al.*, A tweezer array with 6100 highly coherent atomic qubits, *arXiv* (2024), arXiv:2403.12021 [quant-ph].
 - [11] Young, A. *et al.*, Half-minute-scale atomic coherence and high relative stability in a tweezer clock, *Nature* **588**, 408 (2020).
 - [12] Finkelstein, R. *et al.*, Universal quantum operations and ancilla-based read-out for tweezer clocks, *Nature* **634**, 321 (2024).
 - [13] Cao, A. *et al.*, Multi-qubit gates and Schrödinger cat states in an optical clock, *Nature* **634**, 315 (2024).
 - [14] J. P. Covey, H. Weinfurter, and H. Bernien, Quantum networks with neutral atom processing nodes, *npj Quantum Information* **9**, 90 (2023).
 - [15] L. Hartung, M. Seubert, S. Welte, E. Distante, and G. Rempe, A quantum-network register assembled with optical tweezers in an optical cavity, *Science* **385**, 179 (2024).
 - [16] Grinkemeyer, B. *et al.*, Error-detected quantum operations with neutral atoms mediated by an optical cavity, *Science* **387**, 1301 (2025).
 - [17] L. Pause, T. Preuschoff, D. Schäffner, M. Schlosser, and G. Birkel, Reservoir-based deterministic loading of single-atom tweezer arrays, *Phys. Rev. Res.* **5**, L032009 (2023).
 - [18] Norcia, M. *et al.*, Iterative Assembly of ^{171}Yb Atom Arrays with Cavity-Enhanced Optical Lattices, *PRX Quantum* **5**, 030316 (2024).
 - [19] Gyger, F. *et al.*, Continuous operation of large-scale atom arrays in optical lattices, *Phys. Rev. Res.* **6**, 033104 (2024).
 - [20] K. Singh, S. Anand, A. Pocklington, J. T. Kemp, and H. Bernien, Dual-Element, Two-Dimensional Atom Array with Continuous-Mode Operation, *Phys. Rev. X* **12**, 011040 (2022).
 - [21] A. D. Ludlow, M. M. Boyd, J. Ye, E. Peik, and P. O. Schmidt, Optical atomic clocks, *Rev. Mod. Phys.* **87**, 637 (2015).
 - [22] Bluvstein, D. *et al.*, Architectural mechanisms of a universal fault-tolerant quantum computer, *arXiv preprint arXiv:2025* (2025).
 - [23] Baranes, G. *et al.*, Leveraging Atom Loss Errors in Fault Tolerant Quantum Algorithms, *arXiv* (2025), 2502.20558 [quant-ph].
 - [24] Zhang, Z. *et al.*, A high optical access cryogenic system for Rydberg atom arrays with a 3000-second trap lifetime, *arXiv* (2024), 2412.09780 [physics.atom-ph].
 - [25] C. A. Pattison, G. Baranes, J. P. B. Ataiades, M. D. Lukin, and H. Zhou, Fast quantum interconnects via constant-

- rate entanglement distillation, [arXiv \(2024\)](#), 2408.15936 [quant-ph].
- [26] B. M. Terhal, Quantum error correction for quantum memories, [Reviews of Modern Physics](#) **87**, 307 (2015).
 - [27] J. Preskill, Fault-tolerant quantum computation, [arXiv \(1997\)](#), quant-ph/9712048 [quant-ph].
 - [28] Biedermann, G. W. *et al.*, Zero-Dead-Time Operation of Interleaved Atomic Clocks, [Phys. Rev. Lett.](#) **111**, 170802 (2013).
 - [29] Schioppo, M. *et al.*, Ultrastable optical clock with two cold-atom ensembles, [Nature Photonics](#) **11**, 48 (2017).
 - [30] S. Okaba, R. Takeuchi, S. Tsuji, and H. Katori, Continuous generation of an ultracold atomic beam using crossed moving optical lattices, [Phys. Rev. Appl.](#) **21**, 034006 (2024).
 - [31] Cline, J. R. K. *et al.*, Continuous Collective Strong Coupling of Strontium Atoms to a High Finesse Ring Cavity, [Phys. Rev. Lett.](#) **134**, 013403 (2025).
 - [32] Chen, C.-C. *et al.*, Continuous Bose–Einstein condensation, [Nature](#) **606**, 683 (2022).
 - [33] Hu, B. *et al.*, Site-selective cavity readout and classical error correction of a 5-bit atomic register, [arXiv \(2024\)](#), 2408.15329 [quant-ph].
 - [34] S. J. M. Kuppens, K. L. Corwin, K. W. Miller, T. E. Chupp, and C. E. Wieman, Loading an optical dipole trap, [Phys. Rev. A](#) **62**, 013406 (2000).
 - [35] J. Trisnadi, M. Zhang, L. Weiss, and C. Chin, Design and construction of a quantum matter synthesizer, [Review of Scientific Instruments](#) **93**, 083203 (2022).
 - [36] Klostermann, T. *et al.*, Fast long-distance transport of cold cesium atoms, [Phys. Rev. A](#) **105**, 043319 (2022).
 - [37] Matthies, A. J. *et al.*, Long-distance optical-conveyor-belt transport of ultracold ^{133}Cs and ^{87}Rb atoms, [Phys. Rev. A](#) **109**, 023321 (2024).
 - [38] N. Schlosser, G. Reymond, and P. Grangier, Collisional Blockade in Microscopic Optical Dipole Traps, [Phys. Rev. Lett.](#) **89**, 023005 (2002).
 - [39] Comparat, D. *et al.*, Optimized production of large Bose-Einstein condensates, [Phys. Rev. A](#) **73**, 043410 (2006).
 - [40] C. H. Chow, B. L. Ng, V. Prakash, and C. Kurtsiefer, Fano resonance in excitation spectroscopy and cooling of an optically trapped single atom, [Phys. Rev. Res.](#) **6**, 023154 (2024).
 - [41] Savoie, D. *et al.*, Interleaved atom interferometry for high-sensitivity inertial measurements, [Science Advances](#) **4**, 10.1126/sciadv.aau7948 (2018).
 - [42] Chikkatur, A. P. *et al.*, A Continuous Source of Bose-Einstein Condensed Atoms, [Science](#) **296**, 2193 (2002).
 - [43] Wang, S. *et al.*, Accelerating the Assembly of Defect-Free Atomic Arrays with Maximum Parallelisms, [Phys. Rev. Appl.](#) **19**, 054032 (2023).
 - [44] Lin, R. *et al.*, AI-Enabled Rapid Assembly of Thousands of Defect-Free Neutral Atom Arrays with Constant-time-overhead, [arXiv \(2024\)](#), arXiv:2412.14647 [quant-ph].
 - [45] A. Holman and *et al.*, Trapping of Single Atoms in Metasurface Optical Tweezer Arrays, [arXiv \(2024\)](#), 2411.05321 [physics.atom-ph].
 - [46] Xu, Q. *et al.*, Constant-overhead fault-tolerant quantum computation with reconfigurable atom arrays, [Nature Physics](#) **20**, 1084 (2024).
 - [47] N. P. Breuckmann and J. N. Eberhardt, Quantum Low-Density Parity-Check Codes, [PRX Quantum](#) **2**, 040101 (2021).
 - [48] Bravyi, S. *et al.*, High-threshold and low-overhead fault-tolerant quantum memory, [Nature](#) **627**, 778 (2024).
 - [49] Muniz, J. A. *et al.*, Repeated ancilla reuse for logical computation on a neutral atom quantum computer, [arXiv \(2025\)](#), 2506.09936 [quant-ph].
 - [50] Li, Y. *et al.*, Fast, continuous and coherent atom replacement in a neutral atom qubit array, [arXiv \(2025\)](#), 2506.15633 [quant-ph].
 - [51] Kim, D. *et al.*, Large-scale uniform optical focus array generation with a phase spatial light modulator, [Opt. Lett.](#) **44**, 3178 (2019).
 - [52] H. Kim, M. Kim, W. Lee, and J. Ahn, Gerchberg-Saxton algorithm for fast and efficient atom rearrangement in optical tweezer traps, [Opt. Express](#) **27**, 2184 (2019).
 - [53] Ebadi, S. *et al.*, Quantum phases of matter on a 256-atom programmable quantum simulator, [Nature](#) **595**, 227 (2021).
 - [54] Tomita, T. *et al.*, Atom camera: Super-resolution scanning microscope of a light pattern with a single ultracold atom, [arXiv \(2024\)](#), 2410.03241 [physics.atom-ph].
 - [55] Rosi, S. *et al.*, Λ -enhanced grey molasses on the D2 transition of Rubidium-87 atoms, [Scientific Reports](#) **8**, 1301 (2018).
 - [56] M. Walhout, J. Dalibard, S. L. Rolston, and W. D. Phillips, $\sigma^+ - \sigma^-$ Optical molasses in a longitudinal magnetic field, [J. Opt. Soc. Am. B](#) **9**, 1997 (1992).
 - [57] S. K. Pampel, M. Marinelli, M. O. Brown, J. P. D’Incao, and C. A. Regal, Quantifying Light-Assisted Collisions in Optical Tweezers across the Hyperfine Spectrum, [Phys. Rev. Lett.](#) **134**, 013202 (2025).
 - [58] Levine, H. *et al.*, Dispersive optical systems for scalable Raman driving of hyperfine qubits, [Phys. Rev. A](#) **105**, 032618 (2022).
 - [59] Neuhaus, L. *et al.*, Python Red Pitaya Lockbox (PyRPL): An open source software package for digital feedback control in quantum optics experiments, [Review of Scientific Instruments](#) **95**, 033003 (2024).

METHODS

Vacuum System

A simplified schematic of our vacuum system is shown in ED Fig. 1a. The system consists of a MOT chamber and a science chamber, separated by a custom-designed differential pumping tube (DPT, Limit Vacuum Technology) with a 1.5 mm back aperture and 4.3 mm front aperture. The DPT maintains a pressure differential between the two chambers and blocks most of the MOT light. Both DPT and MOT chamber are tilted by approximately 4° to prevent direct scattering of cooling light onto the atomic array in the science chamber, where the line-of-sight passes about 1 cm above the array location. The MOT chamber is primarily composed of a glass cell (Precision Glassblowing) with two rubidium dispenser arms (not shown in ED Fig. 1). The science chamber features a double-sided anti-reflection-coated glass cell (Akatsuki Technology Co. Ltd) with optical contact technology. In both chambers, the pressure remains below the measurable threshold of the ion pumps (SAES NEX Torr and Agilent StarCell 75). Several components are omitted from the figure for clarity, including in-vacuum electrodes (not used in this work) and a vacuum viewport, which provides optical access to the in-vacuum mirror.

Objective & Imaging System

The experimental setup features a high-NA optical system, which enables high-efficiency imaging and tight trapping of single atoms over a field-of-view of more than 1.5 mm diameter (ED Fig. 2a). At its core are two NA=0.65 objectives (Special Optics, custom-design). One of the objectives is used for projecting optical tweezers, and the other for single-atom imaging. The two objectives maintain diffraction-limited performance across the entire field-of-view for wavelengths ranging from 780 to 860 nm. The objective's optical transmission is 92%, and we estimate the total absorption to be $\sim 1\%$ (taking into account finite reflection at each AR-coated surface), which reduces thermal lensing and enables higher trapping laser power in the future.

For single-atom imaging, we use two 4-f telescopes (one high-NA objective and three relay lenses) to map the atomic plane inside the glass cell onto a low-noise CMOS camera (Hamamatsu C15550-20UP). The imaging system magnification is 7.6, such that the fluorescence of a single atom is mapped onto $\approx 3 \times 3$ camera pixels. The quantum efficiency of the CMOS camera at the 780 nm imaging wavelength is $\sim 50\%$. All relay lenses used in the objective beam path (both for imaging and tweezer projection) are custom-designed (Special Optics) to accommodate the large field-of-view.

Tweezer Generation

For optical tweezer projection, we use polarizing beam-splitters (PBS) and dichroic beamsplitters to combine three separate beam paths powered by three high-power

lasers: a 15 W 828 nm fiber amplifier system (Precilaser, 1563 nm + 1762 nm SFG) that generates the dynamic optical tweezers for atom transport, and two 15 W 852 nm fiber amplifier systems (Precilaser, 1544 nm + 1901 nm SFG) that each form the backbone static tweezer array in the preparation and storage zones (ED Fig. 2a).

The 828 nm dynamic tweezers beam path, dedicated to atom transport and sorting, consists of two perpendicularly mounted AODs (G&H AODF 4085) separated by a 1-to-1 4-f telescope. Another 4-f system maps the AOD aperture to the Fourier plane of the objective. The AOD-generated tweezers have a waist of ≈ 800 nm and travel range of $600 \mu\text{m}$ in each dimension on the atom plane. Depending on the transport pattern required, we dynamically switch between different tweezer configurations within one cycle of the experiment. When extracting atoms from the reservoir to the preparation zone, we use 1,440 tweezers at $4.5 \mu\text{m}$ spacing with average depth of $450 \mu\text{K}$. To transport sorted atoms to, or eject atoms from, the storage zone, we generate an array of 540 tweezers at $9 \mu\text{m}$ spacing with an average depth of $600 \mu\text{K}$. We empirically find a reduction in tweezer lifetime as we reduce AOD tweezer spacing, potentially due to atom heating from beating between residual optical potentials of neighboring tweezers.

Static optical tweezer arrays in the preparation and the storage zones are generated in two separate beam paths by two independent SLMs (Hamamatsu X15213-02R) and then combined on a PBS. Each beam path includes a 4-f relay lens system to map the SLM aperture to the Fourier plane of the objective. The SLM phase pattern is calculated using a variation of the Weighted Gerchberg-Saxton (WGS) algorithm [51], and calculation accelerated with a GPU. We numerically “pad” the SLM with 0’s such that the 2D SLM field array (iteratively optimized using WGS algorithm) is 10×10 times larger than the SLM pixel number, enabling 10 times finer control over tweezer positions [52]. This corresponds to a tweezer positioning precision of 65 nm, which reflects an order of magnitude improvement over the natural diffraction unit of 650 nm.

We find significant tweezer spacing distortion due to non-linear effects across the large array span. To systematically overlap thousands of AOD and SLM tweezers, we run an automated procedure that images both AOD and SLM tweezers on a camera, calculates the displacement between the two sets of tweezers for each site, and feeds back on the target tweezer positions of the WGS algorithm site-by-site. We also apply Zernike polynomials to correct for aberrations in the optical system [53], which increases tweezer trap depth by $\sim 10\%$ post-correction.

SLM diffraction efficiency decreases as the distance to the 0-th order increases. To homogenize our backbone tweezer arrays in the preparation and storage zone, we apply the following two-step procedure. First, when generating optical tweezer arrays using the WGS algorithm, we precompensate for spatially varying diffraction efficiency by including a “sinc” term in the target array [53].

This rough homogenization typically yields 15% to 20% inhomogeneity. Then, we run an atom-based homogenization procedure that relies on site-resolved measurements of tweezer-induced light shifts, which is used to feed back onto the WGS target intensity at each site. In the preparation zone, we measure the tweezer light shift by probing the $F = 2 \rightarrow F' = 2$ transition; in the storage zone, we infer the differential light shift via Ramsey interferometry between the two qubit states [54]. After a few rounds of atom-based feedback, we arrive at 5~6% inhomogeneity in both preparation and storage zone (ED Fig. 2b,c). After aberration correction and homogenization, the average SLM trap depth is 370 μK (270 μK) in the preparation (storage) zone with tweezer waist $\approx 800\text{ nm}$.

MOT & Lattice Loading

The experiment starts with the preparation of an atom reservoir, see ED Fig. 1b. We first load $\approx 10^7$ atoms in a MOT within 80 ms while the first optical lattice conveyor belt (Lattice-1) is overlapped throughout. The MOT light is 23 MHz red-detuned from the hyperfine transition $F = 2 \rightarrow F' = 3$, where F refers to hyperfine levels in the $5S_{1/2}$ ground state and F' to hyperfine levels in the $5P_{3/2}$ excited state. The repumping light, created via modulating a sideband on the cooling light, resonantly drives the $F = 1 \rightarrow F' = 2$ transition. We operate the MOT at a magnetic field gradient of 13 G/cm, and use a 395 nm UV-LED for light-induced atom desorption from the glass cell. After the MOT stage, the MOT light is ramped to lower intensity and $\approx 140\text{ MHz}$ red-detuning over 7 ms for compression of the atomic cloud into the lattice. A brief idle time follows the lattice loading procedure, in which the cooling lights are switched off and the magnetic field is zero-ed. Subsequently, we perform Lambda-Gray Molasses (LGM) [55] at low cooling light intensity, with the carrier frequency placed 30 MHz blue-detuned from the $F = 2 \rightarrow F' = 2$ transition and the coherent repumper sideband on two-photon resonance with the $F = 1 \rightarrow F = 2$ transition between both hyperfine ground states. After $t_{\text{LGM}} = 11\text{ ms}$, we load $\approx 4 \times 10^6$ atoms at temperatures $T \approx 20\text{ }\mu\text{K}$ into Lattice-1 as measured via absorption imaging.

Dual-Lattice Optical Transport

We transport atoms from the MOT to the science region using two angled conveyor belt optical lattices [30, 36, 37]. Both transport lattices are derived from a single Ti:Sapphire laser (Matisse, Spectra-Physics) and $\sim 300\text{ GHz}$ red-detuned from the D_1 line, which is found to be the empirical optimum for our available laser power (ED Fig. 3d,e). Lattice-1 has a Gaussian beam waist of around 330 μm at the position of the MOT and a minimum waist of around 250 μm . Particularly at the position of the DPT, its beam diameter is roughly three times smaller than the DPT aperture. Both conveyor belt lattices are spatially mode-matched at the handover-point, from which the waist of the second conveyor belt lattice (Lattice-2) decreases to a minimum waist of 150 μm

in the microscope field-of-view. Both conveyor belt lattices are created via retro-reflection of their respective incoming beams, which are deflected by two acousto-optical modulators (AOMs) into opposite diffraction orders, then imaged back onto the lattice waist (quad-pass configuration) [35]. Mounting the AOMs perpendicular to each other ensures a circular beam shape and enables optimal overlap with the incoming lattice beam on retro-reflection. The quad-pass efficiency is $(0.88)^4 \approx 60\%$, such that for typical incoming powers $P_{\text{in}} \approx 1\text{ W}$ we achieve lattice depths $U_{\text{lat}} > 500\text{ }\mu\text{K}$ for both conveyor belt lattices across the entire transport distance.

After loading Lattice-1, we linearly ramp the frequency of one of the retro-AOMs to introduce a frequency detuning $\Delta\nu(t)$ between both interfering laser beams, and obtain a conveyor belt lattice moving at velocity $v = \lambda\Delta\nu(t)/2$, with λ the wavelength of the lattice laser [36, 37]. The atom cloud is transported over $\sim 39\text{ cm}$ (ED Fig. 3a) before arriving at the handover-point after $t_{\text{L1}} = 50\text{ ms}$. Here, we transfer the atomic cloud from Lattice-1 to Lattice-2 within $t_{\text{HO}} = 1\text{ ms}$ by a simultaneous and opposite linear intensity ramp of both lattice lights and without applying cooling light during the handover (ED Fig. 3b). Finally, within $t_{\text{L2}} = 21\text{ ms}$, Lattice-2 transports the atoms over another $\sim 17\text{ cm}$ into the microscope field-of-view, where it serves as an atom reservoir. For both conveyor belt lattices, we find optimal transport efficiency for accelerations $a_{\text{lat}} \approx 4,000\text{ m/s}^2$ (ED Fig. 3c) and velocities of 8-10 m/s, limited by AOM bandwidth. Using this scheme, we deliver reservoirs of $\approx 2.5 \times 10^6$ atoms at a temperature around 120 μK into our reloading zone, which corresponds to a $\approx 60\%$ dual-lattice transport efficiency at $6\times$ the original temperature. Most of the observed heating is attributed to the lattice handover, not the long-distance transport.

When periodically replacing the atomic reservoir, we start loading a new MOT directly after the lattice handover and, as such, can deliver a fresh reservoir cloud to the science region every $\approx 150\text{ ms}$. Note that only during the second stage of lattice transport, $t_{\text{L2}} = 21\text{ ms}$, no reservoir is available for loading optical tweezers; however, as described in the main text, this is not a limitation to continuous operation as the qubit preparation procedure typically exceeds t_{L2} .

Compared to a single transport lattice design [36, 37], our dual-lattice architecture offers several advantages: (1) Due to the angle between both transport lattices and the differential pumping tube aperture, we avoid a direct line-of-sight and therefore reduce scattering from the MOT onto qubits already present in the science region. (2) The waist of the second conveyor belt lattice becomes largely independent of overall transport distance, and therefore can be decreased within the field-of-view of the objective. This increases the reservoir density for tweezer loading and also limits the impact of lattice-induced scattering and dipole potentials on other zones. (3) While Lattice-2 is still in active use, atoms in Lattice-1 can be prepared and transported to the handover-point in par-

allel. This enables continuous reservoir replacement and decouples the MOT and science chamber operations.

Tweezer Loading from the Lattice Reservoir

In this work, we load optical tweezers from the dense lattice reservoir without employing additional laser cooling during the loading process. Here, we briefly discuss our current understanding of the underlying mechanisms, and outline the effect of loading and extracting tweezers from an active reservoir. In our parameter regime, we expect two mechanisms to contribute to our tweezer loading: *Stochastic* and/or *collisional* loading. Both critically depend on atomic density $n(r, z)$ in the reservoir, which is a function of atom number N per lattice site, atom temperature T , and both radial and axial trapping frequencies ω_r and ω_z . Within one lattice site, it is given by

$$n(r, z) = n_0 \exp\left(-\frac{m}{2k_B T} (w_r^2 r^2 + w_z^2 z^2)\right)$$

with $n_0 = N\omega_z^2 \omega_r (m/(2\pi k_B T))^{3/2}$ the peak density, m the mass of ^{87}Rb , r the radial distance from the center of the reservoir, and z the axial distance from the lattice site. The tweezers are far smaller than the radial dimension of the reservoir but larger than the axial lattice spacings. We therefore assume the reservoir density to be constant along r and calculate densities $\langle n(r) \rangle_{\text{lat}}$ that are averaged over the axial direction of the lattice, denoted as $\langle \rangle_{\text{lat}}$. For our reservoir parameters, we estimate an atom density of $\langle n(r=0) \rangle_{\text{lat}} \approx 10^{12} \text{ cm}^{-3}$. Neglecting dependencies on atom temperature and the relative trap depth between the lattice and tweezers, we now turn to a brief discussion of both loading mechanisms.

Stochastic loading: When snapping on the tweezer, the probability to stochastically capture an atom from the center of the reservoir can be approximated as $P_{st} \propto V_{\text{twz}} \langle n \rangle_{\text{lat}}$, where V_{twz} is the effective tweezer volume.

Collisional loading: An atom moving through a background gas collides with a rate $\Gamma(r, z) = n(r, z)v_{\text{rel}}\sigma$, with v_{rel} the thermal relative velocity between two atoms, and σ the scattering cross section. The density of collisions is given by $\gamma(r, z) = \frac{1}{2}n(r, z)^2 v_{\text{rel}}\sigma$, and therefore the probability to collisionally load an atom will be proportional to $P_{\text{col}} \propto \langle \gamma \rangle_{\text{lat}} V_{\text{twz}} \Delta t$, with Δt the tweezer-lattice overlap time [39].

In our experiments, we efficiently load optical tweezers from the reservoir with $\sim 50\%$ single-atom filling fractions (i.e., saturated loading) by simply switching on tweezers and immediately transporting captured atoms out of the active reservoir (Fig. 1b). Since we are transporting atoms perpendicular to the axial lattice potential, we observe no difference in survival when moving atoms through the active reservoir versus in free-space as a function of tweezer velocity [19] (ED Fig. 4b). On average, we find that ≈ 5 atoms are lost from the reservoir per extracted tweezer by comparing atom number in the reservoir with the number of atoms obtained via extraction. Note that this does not necessarily imply *loading* of 5 atoms

into the tweezer per extraction, since we expect that the rather invasive extraction procedure accelerates evaporative losses in the reservoir.

Finite-Field Laser Cooling & Imaging

A key feature of our reloading architecture is the ability to initialize fresh qubits and perform mid-circuit laser cooling and imaging in the presence of a static magnetic field. Avoiding field changes, such as field-zeroing as typically necessary for polarization gradient cooling (PGC), protects coherence in existing qubits and enables faster qubit preparation cycles. To this end, all qubit preparation and manipulation protocols are designed to operate at a fixed magnetic field of 4.2 G, which defines the qubit quantization axis at all times. The preparation zone is illuminated with a pair of 1D counter-propagating 780 nm beams with opposite circular polarizations (σ^+ and σ^-) aligned along the magnetic field axis. The two beams are detuned relative to each other by twice the Zeeman splitting to compensate for the energy shift of hyperfine levels due to the quantization field [56]. We use this architecture for laser cooling, imaging, parity-projection, and qubit state initialization as shown schematically in ED Fig. 5a, with cooling and imaging performing comparably to the zero-field configuration.

To begin qubit preparation on atoms extracted into the preparation zone from the reservoir, an explicit parity-projection pulse is required since our loading mechanism typically results in more than one atom loaded per tweezer. Before ramping up SLM tweezers in the preparation zone, we perform PGC with light 60 MHz red-detuned from $F = 2 \rightarrow F' = 3$ to induce pair-wise atom losses in AOD tweezers via light-assisted collisions [57]. After 10 ms, we handover atoms to the SLM array and observe roughly 50% occupation and less than 1% of sites with more than one atom. This parity-projection step therefore sets an upper bound on imaging survival and is crucial for obtaining well-separated imaging histograms. Additionally, we observe atoms trapped in out-of-plane potentials created by the SLM (Talbot effect), which we remove with a brief resonant push-out pulse [10].

Fast, lossless imaging is then used to identify atoms for rearrangement. We image for 10 ms using PGC parameters, which achieves a site-resolved discriminant fidelity of 99.99% with a survival probability of 99.5% (ED Fig. 5b). Higher imaging fidelity and survival can always be achieved by imaging longer at larger detuning or weaker powers. Our 1D counter-propagating beam configuration offers the added benefit of a background-free imaging signal, eliminating the need for Fourier filtering since the beams do not directly scatter into the imaging objective. During imaging in particular, we observe that atoms from our lattice reservoir occasionally leak into the nearby preparation zone, which are then trapped into tweezers by imaging/cooling light. We avoid this by moving our lattice reservoir roughly a centimeter away from the objective field-of-view after every tweezer extraction cycle, and move it back before the next cycle.

If not accounted for, lattice spilling and improper parity-projection can each decrease imaging survival by $\sim 5\%$, with the exact number dependent on reservoir density and imaging duration.

During the 20 ms to 40 ms of rearrangement, we apply laser cooling via electromagnetically-induced transparency (EIT) [40]. We use the same laser and beam geometry, except in a strong “coupling” and weak “probe” configuration, operating on a two-photon resonance 70 MHz blue-detuned from $F = 2 \rightarrow F' = 2$ [40] with intensity ratio 13:1. We probe atom temperature via drop-recapture and extract radial temperatures of 12 μK (ED Fig. 5c). A complementary adiabatic trap ramp-down measurement, which is more sensitive to axial temperatures, yields comparable results despite limited \mathbf{k} -vector projection of the cooling light along the tweezers’ axial direction. All cooling lights (PGC and EIT) contain a repumper frequency addressing the $F = 1 \rightarrow F' = 2$ transition, created by modulating an electro-optic modulator (EOM) at ~ 6.8 GHz.

Atom Rearrangement

After stochastically loading the preparation zone 120×12 tweezer array, we rearrange the atoms into a defect-free array of typically 540 sites, except for the qubit flux demonstration in Fig. 1c where we arrange to 600 sites. The same 2D AOD pair used for extracting atoms from the lattice reservoir performs rearrangement, controlled by a dedicated arbitrary waveform generator (AWG, Spectrum Instrumentation M4i.6631-x8). Leveraging our unique large-aspect-ratio preparation zone geometry, we execute efficient row-by-row sorting (ED Fig. 6a). In each row, a single parallel move fills all empty target sites using available atoms while navigating through inter-row gaps to avoid backbone SLM traps. Each row takes 700 μs to sort, with EIT cooling active throughout.

To optimize real-time processing, we precompute all possible move segments as waveform chirps. During each experiment, the rearrangement program selectively synthesizes the precomputed waveform chirps based on the specific atom loading information of that shot (provided by a real-time image analysis program). We exploit the AWG’s FIFO mode to reduce latency from waveform calculation. Since each row’s sorting is independent, we stream its waveform as soon as it is computed while moves for the next row are calculated in parallel. This reduces calculation latency by over an order of magnitude. Under optimal conditions, we allocate ≈ 20 ms for rearrangement which takes into account data transfer latency, row-by-row sorting time, and a small buffer to accommodate program runtime fluctuations. For all sequences involving storage zone operation, we increase the camera ROI to include the storage zone, which increases latency (and therefore the time allocated for rearrangement) by ~ 10 -20 ms. This large ROI is unnecessary for future continuous operations (e.g., for error-correcting circuits), where imaging is confined to the preparation zone and not required in the storage zone.

For 540-site rearrangement, we achieve an averaged target array filling fraction of 99.6% (ED Fig. 6b), primarily limited by imaging survival. Given our vacuum lifetime of over 150 s, losses from background gas collisions contribute less than 0.1% to the rearrangement infidelity. ED Fig. 6a (lower) showcases a single-shot preparation zone fluorescence image of a defect-free array after rearranging to 600 sites. Atoms remaining outside the target array are automatically discarded when the subarray is transported to (re)load the storage zone. We intentionally rearrange into every other column, creating a sparse array geometry that reduces the average atom travel distance during sorting, thereby improving both rearrangement fidelity and speed.

Storage Array Building

One of the key considerations in assembling large-scale atom arrays is the trade-off between increasing tweezer spacing in order to minimize inter-tweezer crosstalk, and decreasing tweezer spacing for higher SLM diffraction efficiency. Therefore, our 3,240-site storage zone tweezer array features alternating horizontal spacings: wide, 6 μm -channels for minimal AOD-SLM tweezer crosstalk during atom transport through the array, and smaller spacings of 3 μm in order to pack the array close to the SLM 0-th order where diffraction efficiency is significantly higher. The entire array is placed on one side (two quadrants) of the SLM 0-th order, as we empirically find that having large tweezer arrays in all four quadrants introduces additional ghost optical spots between tweezers.

The 90×36 -site storage array is divided into six interleaved subarrays of 45×12 sites. Subarrays feature regular tweezer spacings of 9 μm and are filled sequentially, such that the entire storage array is assembled in six iterations (ED Fig. 6d). Within each iteration, we first load the preparation zone array stochastically, then rearrange atoms into a 540-site target array with a spacing of 9 μm horizontally and 4.5 μm vertically. Afterwards, atoms are picked up by AOD tweezers and transported to one of the six subarrays (see Supplementary Movie). During this transport, the subarray is vertically expanded from 4.5 μm to match the 9 μm spacing in the storage zone, while the horizontal spacing remains at 9 μm . Maintaining identical horizontal spacings throughout the transport minimizes expansion overhead and enables faster transport. In addition, the sparse subarray structure largely avoids AOD heating at closer spacings.

We observe a slightly lower atom survival probability during tweezer transport to the storage zone when the static lattice reservoir is present, which can be recovered when the lattice potential itself is in motion simultaneously. As described previously, the lattice reservoir is translated by 1 cm out of the objective field-of-view to avoid lattice spilling during high-contrast imaging, and moved back before the next tweezer extraction cycle. Therefore, we now simply time atom movement to the storage zone to occur synchronously with moving the lattice reservoir back into the objective field-of-view,

thereby mitigating the above effect. ED Fig. 6c shows storage zone assembly statistics after 300 repeated trials; on average, we load 3,193 atoms out of 3,240 sites, corresponding to a loading fraction of 98.5%.

Qubit Initialization

After rearranging a defect-free array, we initialize the atoms into their qubit subspace. The qubit subspace is spanned by the two hyperfine clock states in the ground-state manifold of ^{87}Rb , which we define as $|F=1, m_F=0\rangle \equiv |0\rangle$ and $|F=2, m_F=0\rangle \equiv |1\rangle$. To prepare the atoms in state $|0\rangle$, we leverage the previously discussed 1D local beam configuration. Both of the counter-propagating preparation zone beams simultaneously address the $F=1 \rightarrow F'=0$ and $F=2 \rightarrow F'=2$ transitions. By selection rules, state $|0\rangle$ is dark to the σ^\pm circularly polarized light field addressing $F=1 \rightarrow F'=0$, while the states $|F=1, m_F=\pm 1\rangle$ are optically pumped to $|0\rangle$ through $|F'=0, m_{F'}=0\rangle$. Simultaneously, atoms in states $F=2$ are depumped into $F=1$ by addressing the $F=2 \rightarrow F'=2$ transition (ED Fig. 5d). We observe a $1/e$ -time of $5\mu\text{s}$ for populating state $|0\rangle$. This technique for fast state initialization is advantageous as it requires only few scattered photons, minimizing heating from scattering, while simultaneously avoiding magnetic field rotations [4]. From the preparation zone Rabi contrast, we infer a state preparation and measurement (SPAM) fidelity of 98.1(3)%, likely limited by polarization impurities and off-resonant scattering to other hyperfine levels in the excited state. The state preparation fidelity can potentially be improved by incorporating Raman-assisted optical pumping schemes [4].

Qubit Manipulation and Readout

We drive the qubit states via optical Raman transitions, in a setup similar to [58] but operating 400 GHz blue-detuned from the 780 nm transition. The Raman beam drives the qubits at Rabi frequency $\Omega/2\pi \approx 1\text{ MHz}$. At this intensity, we measure a T_1 -like scattering lifetime of 10 ms, in agreement with *ab initio* Raman scattering calculations. From this, we infer a scattering-limited fidelity of 0.99995 per π -pulse. We note, however, that this represents an upper bound on our single-qubit gate fidelity; in practice, additional error sources such as atomic decoherence, intensity fluctuations, and phase noise may also contribute [10]. The Raman beam is shaped to homogeneously address qubits in the large storage zone, which is achieved by using a fixed holographic phase plate (HOLO/OR ST-268) that forms a top-hat beam profile across the extent of the array. From measuring row-by-row Rabi frequency, we infer a beam homogeneity of approximately 1.04% root-mean-square variation and 3.4% peak-to-peak variation on the atoms (ED Fig. 7a). To minimize crosstalk between the Raman beam and the atoms in the preparation zone, we knife-edge the beam tail at the intermediate imaging plane of the beam shaping telescope, and thus remove residual light in the preparation zone.

To selectively read out qubits in $|0\rangle$, we apply a pushout pulse that resonantly removes atoms in $F=2$ from the trap, then image atoms that remain in the $F=1$ ground-state manifold. To readout qubits in $|1\rangle$, we first apply a π -pulse to rotate the population to $|0\rangle$, followed by the same pushout and imaging pulse. We follow a slightly different imaging procedure depending on where atomic qubits are read out. In the preparation zone, we use PGC for qubit readout under a *static* magnetic field, which, in this work, is primarily used to identify occupied tweezer sites for atom rearrangement, but can also serve as mid-circuit readout in future error correction protocols. For global readout of all storage array qubits at the end of the experiment, we use a separate retro-reflected circularly-polarized global imaging beam at *zero* magnetic field.

Qubit Shielding

Throughout the experiment and particularly during qubit preparation, we protect the $5S_{1/2}$ ground-state qubits in the storage zone from near-resonant photon scattering with the $5S_{1/2} \rightarrow 5P_{3/2}$ transition by addressing the $5P_{3/2} \rightarrow 4D_{5/2}$ transition near 1529 nm [33]. This results in an effective light-shift of the D₂-line, which is now out of resonance to the imaging and cooling light applied to nearby qubits (“shielding”). We estimate a suppression of scattering by a factor of $\sim 1,000$.

The shielding light is sourced from a single-frequency fiber laser (Connet CoSF-D) outputting up to 10 Watts at 1529.6 nm, which is passed through an AOM (G&H 3165-1) for fast switching control and fiber-coupled onto the experimental table. Similar to the Raman beam, we shape the shielding beam with a holographic phase plate (HOLO/OR ST-356) to create a flat-top beam profile of $\approx 250\mu\text{m}$ along the vertical extent of the storage zone array. The beam tails are knife-edged in an intermediate imaging plane to ensure no shielding crosstalk onto the preparation zone. The knife-edged flat-top beam profile is shown in ED Fig. 7b. In a spectroscopy scan, we step the 1529 nm-wavelength during simultaneous imaging and low-power shielding of storage zone atoms and resolve the $4D_{5/2}$ resonance by suppression of global imaging signal. To further optimize shielding performance, we maximize the T_2 -time of storage qubits as a function of shielding wavelength while locally imaging qubits in the preparation zone (Fig. 3c). In practice, the shielding light is operated free-running in wavelength with approximately 2.5 W onto the atoms.

Maintaining Coherence while Reloading

In Fig. 3a, we apply N-pulses as part of a repeated XY16 dynamical decoupling (DD) pulse sequence (denoted as XY16-N) with fixed pulse spacing $2\tau \approx 1.6\text{ ms}$. During DD, we measure storage qubit coherence under various conditions: First, we quantify the effect of the distant MOT on storage qubits when pulsing the MOT at a 30% duty cycle with the lattice reservoir lights off. This particular duty cycle is chosen to replicate typical MOT

loading cycles in our continuous qubit reloading protocol. Second, we additionally switch on the preparation zone imaging light while the reservoir is present for the entire probing duration to simulate the effect of concurrent local qubit preparation. We observe no difference between turning on local imaging light with atoms present in the preparation zone versus without, suggesting that the primary source of decoherence during qubit preparation arises from scattered light originating from the optics and apparatus, rather than from photons scattered by atoms in the preparation zone. Lastly, we shield storage zone qubits while the distant MOT is loaded and held at saturation, the lattice reservoir is present, and preparation zone imaging light is switched on for the entire probing duration. This simulates the most demanding application of storage array shielding. Complementary to Fig. 3a which measures T_2 -times under the conditions described above, we similarly probe depolarization of storage zone qubits when the qubit is initialized in either $|0\rangle$ (ED Fig. 8a) or $|1\rangle$ (Fig. 3b). Here, in addition to the above variations, we also quantify storage qubit depolarization caused by the lattice reservoir light alone.

Continuous Qubit Reloading

In this section, we detail the experimental sequence used to achieve our results of qubit reloading while maintaining storage qubit coherence shown in Figs. 4b,c,d and ED Figs. 10a,b. A sequence schematic is given in ED Fig. 9. First, we transport a lattice reservoir into the science region, from which tweezers repeatedly extract atoms into the preparation zone. Subsequently loaded lattice reservoirs are transported to the tweezer science region in parallel, such that the reservoir itself is replaced every two tweezer extractions. Once in the preparation zone, atoms undergo the qubit preparation sequence shown in ED Fig. 5a before being transported into the storage zone. The complete qubit preparation sequence, including the move to the storage array, takes a total of ~ 80 ms and constitutes one reloading cycle. After initial assembly of the storage qubit array, we continue preparing newly state-initialized qubit ensembles in the preparation zone, and eject and refill one of six qubit subarrays in the storage zone as described in the main text. To eject a subarray, the qubits are transferred back into overlapped AOD tweezers and accelerated out of the objective field-of-view. Storage subarray ejection takes ≈ 5 ms and occurs simultaneously to the preparation zone image used for atom rearrangement. For Fig. 4b, we loop this qubit reloading sequence for variable time before our global imaging readout. Shielding light is applied to the storage zone during the entire experimental sequence.

For Figs. 4c,d, we additionally apply dynamical decoupling sequences ($X_{\pi/2} - \text{XY16-64} - X_{-\pi/2}$) with a fixed pulse spacing $2\tau \approx 1.1$ ms onto all storage zone qubits during each reloading cycle. Therefore, within each loop, qubits are first rotated $|0\rangle \rightarrow |+\rangle$, then undergo the XY16 decoupling sequence to mitigate dephasing. Before fresh qubits are moved into the storage array

from the preparation zone, we apply a $X_{-\pi/2}$ pulse to map remaining coherence to population by rotating back to state $|0\rangle$. This reloading cycle is repeated a variable number of times, and each subarray is exchanged with a set of fresh qubits every six iterations. In ED Fig. 10a, we supplement main text Fig. 4c by averaging readout probability over the entire storage array instead of analyzing each subarray individually.

Instead of mapping coherence back to $|0\rangle$ population after each reloading cycle, we can also map it to alternating $|0\rangle$ or $|1\rangle$ population by choosing ($X_{\pi/2} - \text{XY16-64} - X_{+\pi/2}$) as cyclic decoupling sequence. This results in subarrays 1, 3, and 5 hosting qubits in superposition state $|+\rangle$ and subarrays 2, 4, and 6 qubits in the opposite state $|-\rangle$ during dynamical decoupling after initial array assembly. When mapped back to population, this yields a checkerboard pattern of qubit states $|1\rangle$ and $|0\rangle$ in the storage array. Analogous to Fig. 4d, this is shown in ED Fig. 10b where the storage array is read out in different qubit bases and each subarray analyzed individually.

Control System and Timing

We use National Instruments (NI) cards to generate digital and analog control signals (NI PXIe-6535 and NI PXIe-6738, respectively) for the laser cooling and trapping stages of our experiment, including the MOT loading, dual-lattice transport, and qubit preparation sequences. For operations that require waveform generation with nanosecond precision, we utilize arbitrary waveform generators (AWGs, Spectrum Instrumentation DN2.663-04) whose output is triggered by the NI cards. In our experiments, AWGs handle timing of single-qubit gates and dynamical decoupling pulses, and supply the chirped waveforms for atom sorting and transport in AOD tweezers.

Our control system is designed to allow for practically unlimited duration of continuous operation. For NI-generated control signals, we calculate and stream the waveform samples on-the-fly to circumvent memory limitations. For AWG-controlled atom transport and dynamical decoupling, we instead store the precalculated waveform in the on-board memory and loop over it for an arbitrary number of times. Here, the dynamical decoupling sequence requires particular care in selecting the signal frequency when looping over the same memory segment as to avoid phase jumps in the IQ-modulated 6.8 GHz microwave signal. More details of our control software will be discussed in an independent manuscript which is currently in preparation.

Calibrating and maintaining intensity of light pulses that are too short for active real-time stabilization is a significant technical challenge in continuously operating experiments. For our optical Raman light, we employ an FPGA-based digital servo with digital sample-and-hold [59] to stabilize pulse intensity, which eliminates analog hold decay, integral windup and enables calibration pulses as short as 5 μ s. This calibration pulse is inserted before every XY16-64 decoupling cycle with the

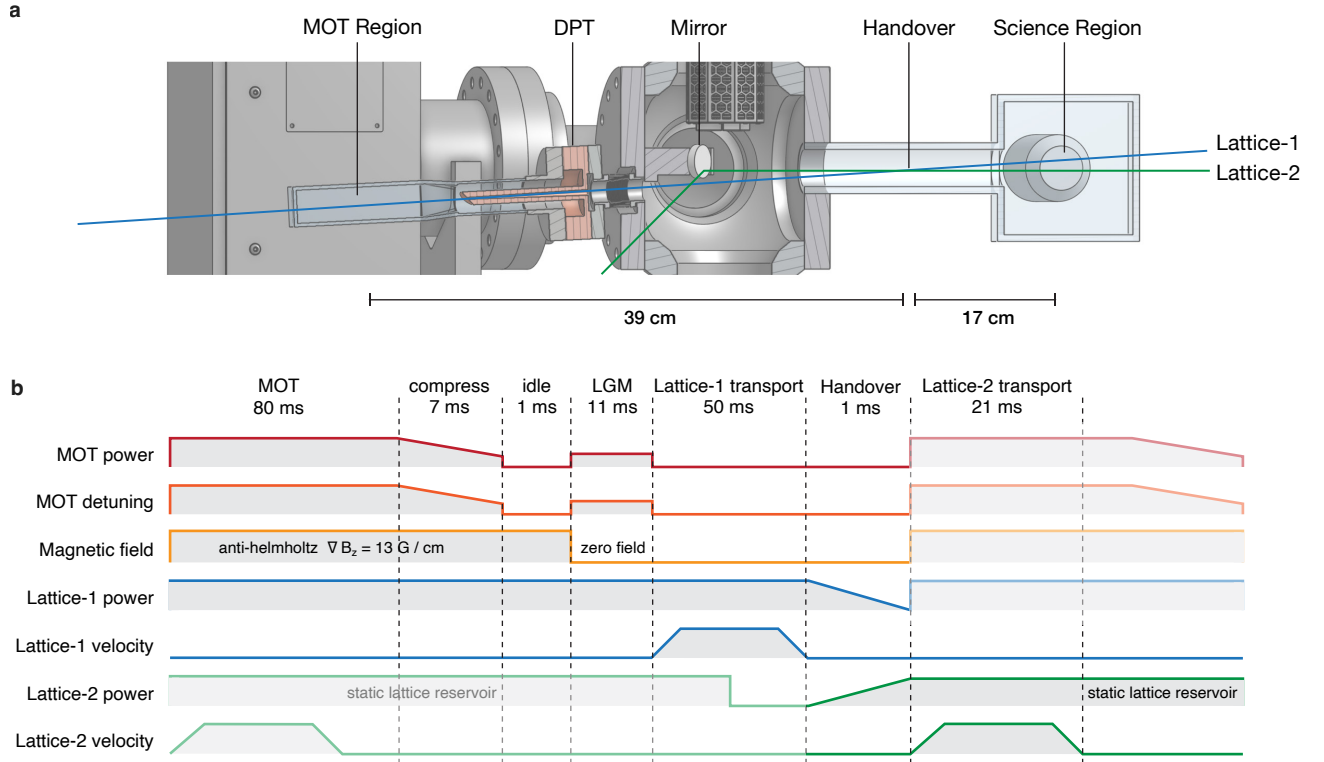
6.8 GHz microwave source detuned by 20 MHz to ensure that qubit states are not driven. Although the calibration pulse flashes onto existing storage qubits, its duration is three orders of magnitude shorter than the ~ 10 ms T_1 -like scattering timescale associated with the Raman light. With the digital hold, we actively stabilize every decoupling cycle *in-situ*, and achieve no long-term decay in pulse intensity and pulse-to-pulse error of $\lesssim 1\%$.

Data Analysis

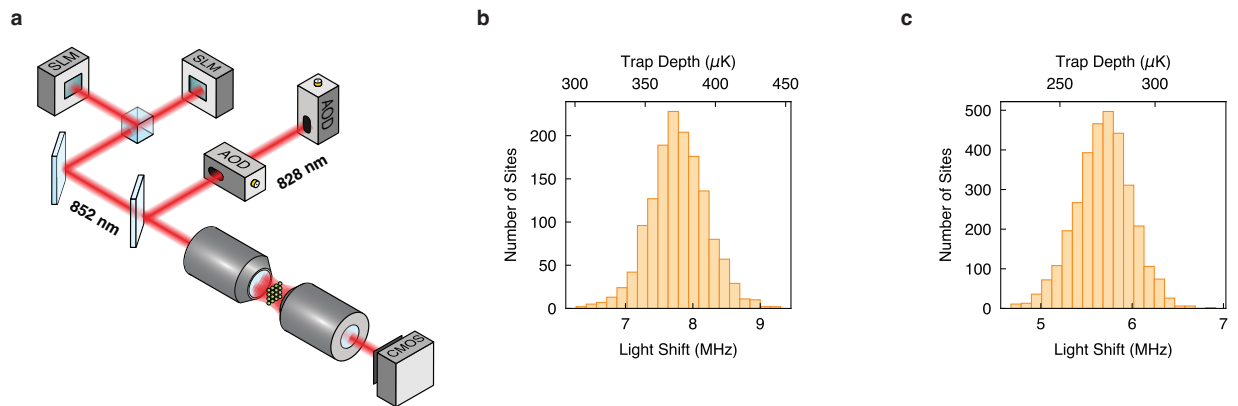
For the measurements in Figs. 3a,b and ED Fig. 8a, we read out the qubit state after the probing duration and define contrast as $(P_0(t) - P_1(t))/(P_a(t) - P_{|m_F \pm 1\rangle}(t = 0))$. Here, $P_0(t)$ ($P_1(t)$) denotes the probability to measure qubits in $|0\rangle$ ($|1\rangle$) at given time t by reading out the $F = 1$ hyperfine level without (with) a preceding π -pulse as described above. $P_a(t)$ is the probability to measure an atom in any state by omitting the pushout pulse before imaging atoms (lifetime measurement). Additionally, we correct for qubits initially populating neighboring Zeeman states $|F = 1, m_F \pm 1\rangle$ at $t = 0$ denoted as $P_{|m_F \pm 1\rangle}(t = 0)$, since we observe 5-10% leakage from state $|0\rangle$ into other m_F states within the $F = 1$ manifold when transporting qubits from the preparation to the storage array using AOD tweezers. This is attributed to RF-tone beating driving the transitions between $|0\rangle \rightarrow |F = 1, m_F \pm 1\rangle$ levels, which can be mitigated by operating at higher quantization fields or fine-tuning the RF tones applied to the AODs in future experiments. To measure $P_{|m_F \pm 1\rangle}(t = 0)$, we isolate qubits in states $|F = 1, m_F \pm 1\rangle$ by first applying a pushout pulse, then a π -pulse to transfer the population $|0\rangle \rightarrow |1\rangle$, followed by a final pushout pulse before readout. For all measurements of Figs. 3a,b and ED Fig. 8a, we fit an exponential decay to the contrast and quote the fitted $1/e$ decay time as T_2 - and T_1 -times, which are presented in ED Fig. 8b.

For the measurements in Figs. 4c,d and ED Fig. 10a,b, “Readout Probability” is defined as $(P_0(t) - P_{|m_F \pm 1\rangle}(t = 0))/(P_a(t) - P_{|m_F \pm 1\rangle}(t = 0))$, where $P_0(t)$ again denotes the probability to measure qubits in $|0\rangle$ at given time t as described above, and $P_a(t)$ the lifetime measurement. For the red-shaded lines in Fig. 4c and ED Fig. 10a, we apply a π -pulse before the measurement. As before, we measure and correct for qubits initially populating neighboring Zeeman states $|F = 1, m_F \pm 1\rangle$ due to state leakage during atom transport. For Fig. 4b, we measure “Polarization Contrast” defined as $(P_0(t) - P_1(t))/(P_a(t) - P_{|m_F \pm 1\rangle}(t = 0))$.

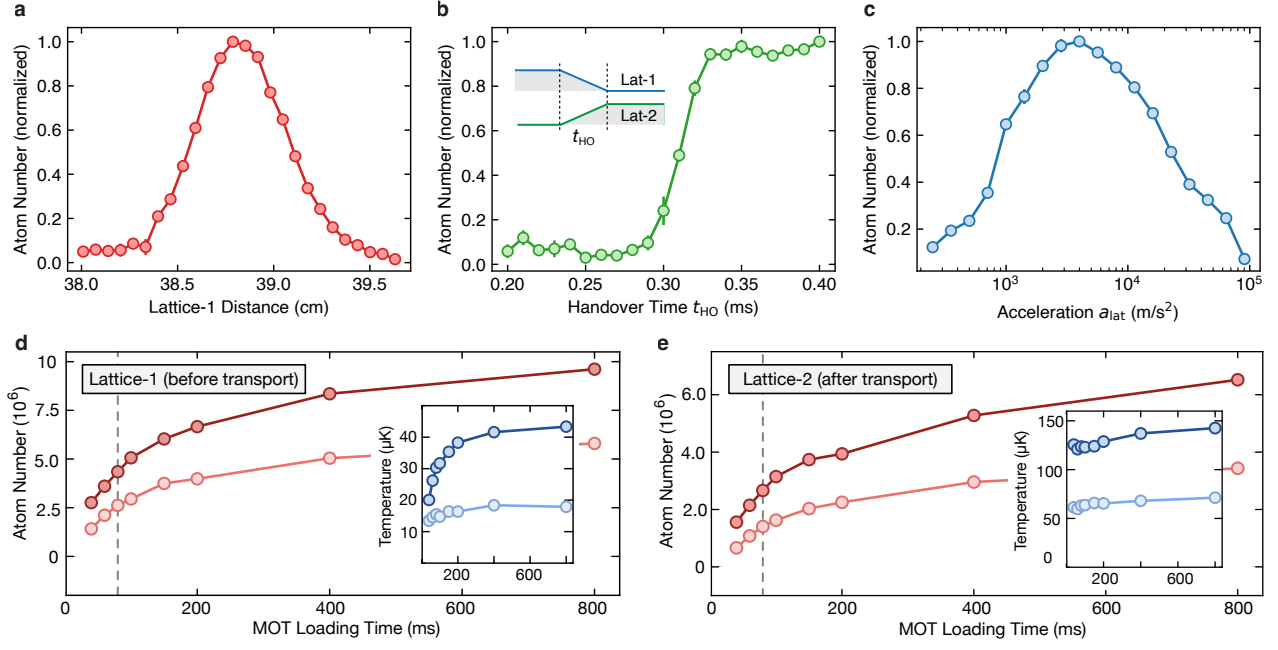
Data Availability The data that supports this study are available from the corresponding author on reasonable request.



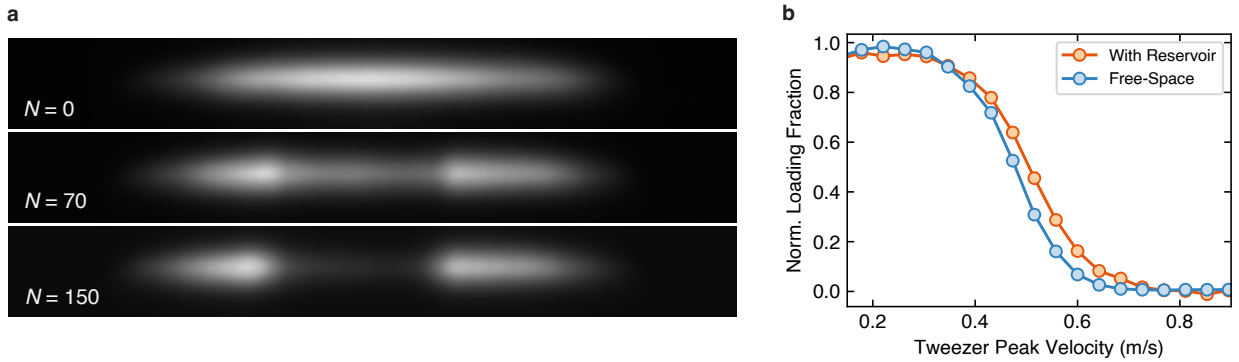
Extended Data Figure 1. **Vacuum chamber and lattice loading sequence.** **a**, Simplified view of the vacuum chamber. Atoms are cooled and loaded from a MOT into an optical lattice (Lattice-1) and then transported through the differential pumping tube (DPT, orange) to the science chamber. The atomic cloud is then handed over to a second optical lattice (Lattice-2), which is reflected out of the chamber by an in-vacuum mirror. While most MOT light is blocked by the DPT, the tilted design between both chambers avoids direct line-of-sight between the computational array and the MOT location. **b**, Summary of the experimental sequence, including the MOT stage, loading and cooling of Lattice-1 as well as lattice transport and handover. After the lattice handover, we restart the lattice loading procedure in the MOT chamber, while Lattice-2 is shipped to the science region where it serves as an atomic reservoir for tweezer extraction. The gray-shaded regions indicate the previous/next lattice loading cycle.



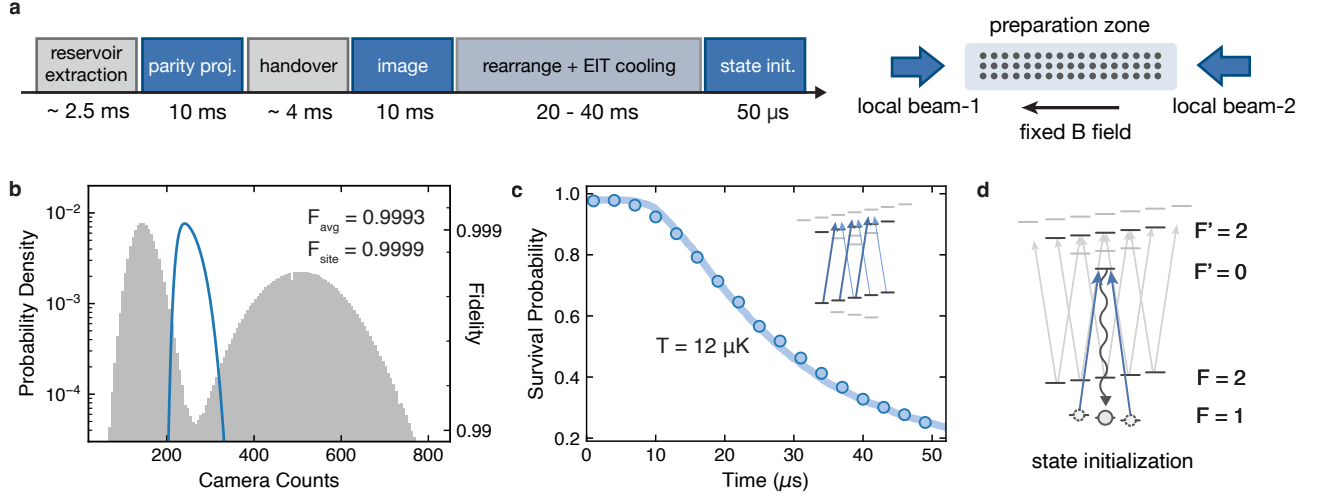
Extended Data Figure 2. **High-NA beam paths and optical tweezer characterization.** **a**, Simplified optical beam paths for tweezer generation and single-atom imaging. Before the tweezer-generation objective, the preparation and storage zone SLMs (both at 852 nm) are combined on a PBS, then further combined with the 828 nm AOD beam path on a dichroic beamsplitter. A second objective is used for single-atom imaging. Relay optics are omitted for simplicity. **b**, **c**, Histograms of trap depth measured for the preparation zone (b) and storage zone (c) tweezer arrays after two-stage homogenization. The preparation (storage) zone tweezers have an average trap depth of 370 μK (270 μK) with standard deviation 5.4% each.



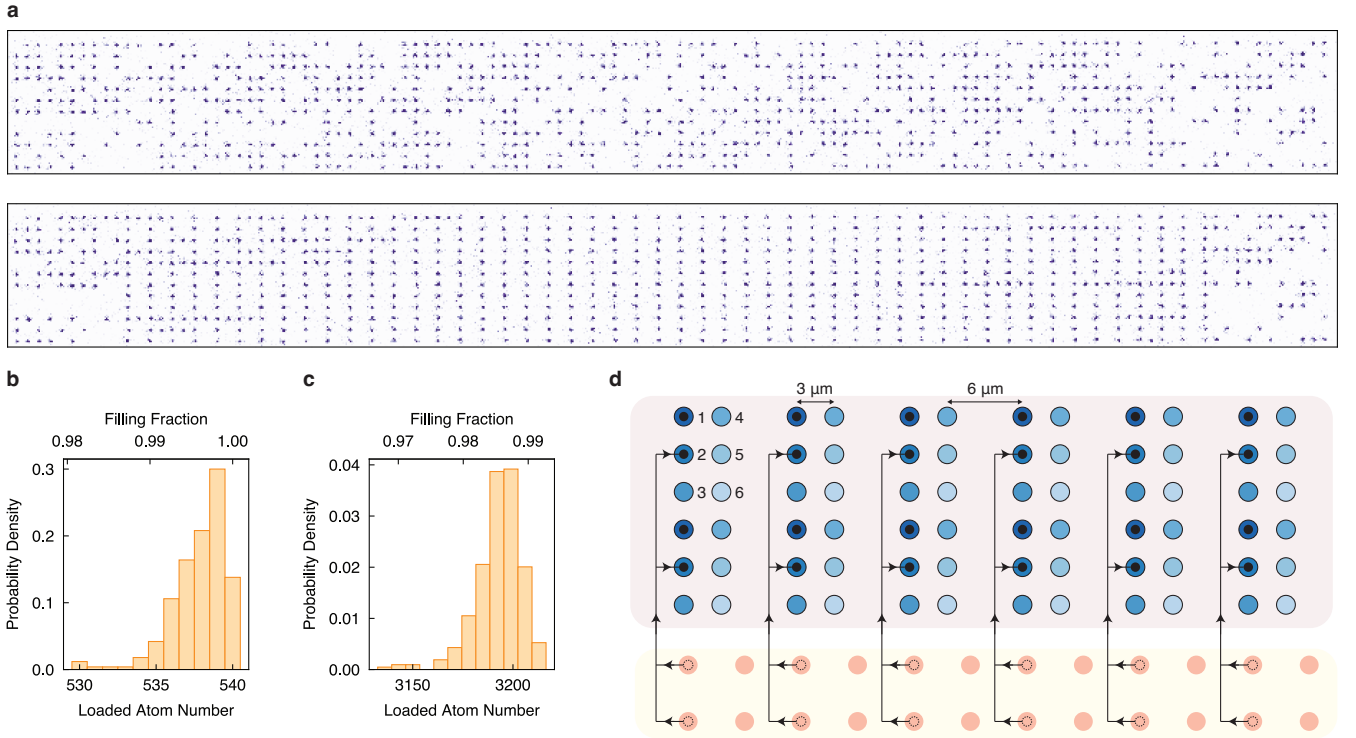
Extended Data Figure 3. **Dual-lattice conveyor belt transport.** **a**, Atom number (normalized) obtained in the reservoir after transport as a function of Lattice-1 travel distance before handing the atomic cloud over to Lattice-2. **b**, Atom number (normalized) obtained in the reservoir as a function of time dedicated for lattice handover, which consists of a simultaneous and opposite ramp of the Lattice-1 and Lattice-2 intensities (see inset schematic). **c**, Atom number (normalized) obtained in the reservoir as a function of conveyor belt acceleration, here shown exemplary for Lattice-1. **d,e**, Atom number (red) and temperature (blue) in the respective transport lattices before (d) and after (e) transport, shown for varying MOT loading times with the lattices ~ 300 GHz red-detuned from the D₁ line (darker color shading). The dashed gray line represents our chosen MOT loading time, which was sufficient to obtain the density required for tweezer loading. The light-shaded curves are measured for further red-detuned lattices (~ 700 GHz), providing lower lattice-induced scattering and colder temperatures but also lower atom numbers.



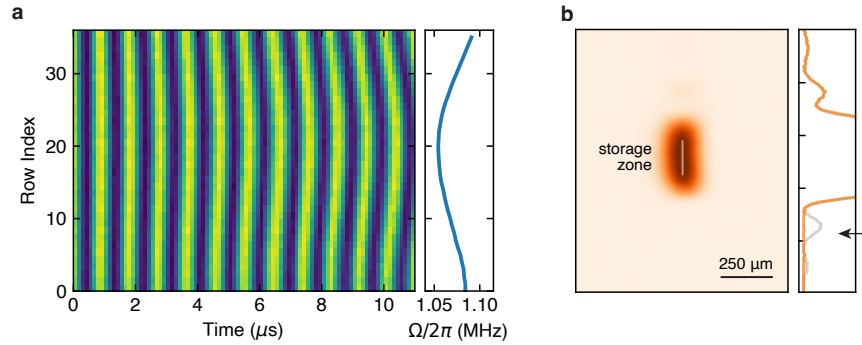
Extended Data Figure 4. **Extracting atoms from the lattice reservoir.** **a**, Single-shot fluorescence images of the lattice reservoir after extracting atoms via optical tweezers for N -repetitions. **b**, Preparation array loading fraction as a function of tweezer velocity during extraction from the reservoir. We find no significant difference when moving atoms perpendicularly through the lattice potential versus in free-space.



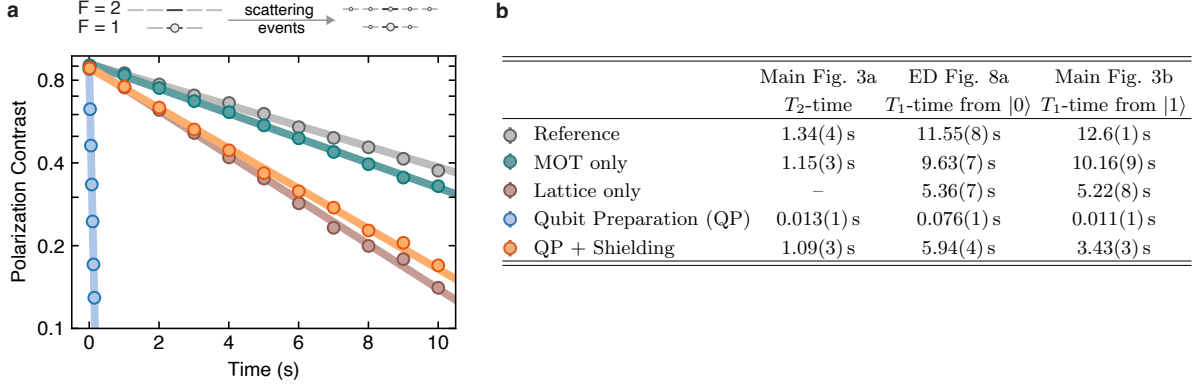
Extended Data Figure 5. **Characterization of the qubit preparation sequence.** **a**, Summary of the experimental sequence for qubit preparation. After extraction from the reservoir, the atoms are transported to the preparation zone within ~ 2.5 ms. Here, a parity-projection pulse of 10 ms is performed to achieve either one or zero atoms per AOD tweezer trap. Atoms are then handed off to a backbone tweezer array generated by an SLM while applying PGC, involving SLM-AOD intensity ramps and a brief ($30 \mu\text{s}$) resonant Talbot plane push-out pulse. A 10 ms fluorescence image is used to identify occupied sites for rearrangement, followed by EIT cooling and simultaneous atom sorting into a defect-free array. Depending on the desired atom configuration, rearrangement takes between 20 ms and 40 ms (largely dominated by data transfer latency). Finally, atoms are optically pumped into the qubit state $|0\rangle$ within $50 \mu\text{s}$. All light pulses are performed by two circularly-polarized counter-propagating laser beams at static magnetic field (schematic). **b**, Imaging histogram for 1D imaging at finite-field. The extracted average discriminant fidelity is 0.9993 with a site-resolved discriminant fidelity of 0.9999. The blue curve visualizes the discriminant fidelity as a function of threshold value. Note that the net imaging fidelity must also account for imaging survival, which limits total fidelity to $\mathcal{F} \sim 0.995$. **c**, Drop-and-recapture measurement of atomic temperature after 40 ms of 1D EIT cooling and subsequent qubit state preparation. The temperature is extracted as $T = 12 \mu\text{K}$ via Monte-Carlo simulations. Inset: Relevant atomic levels for EIT cooling. **d**, Schematic illustrating relevant atomic levels for fast initialization of qubit state $|0\rangle$ under finite field.



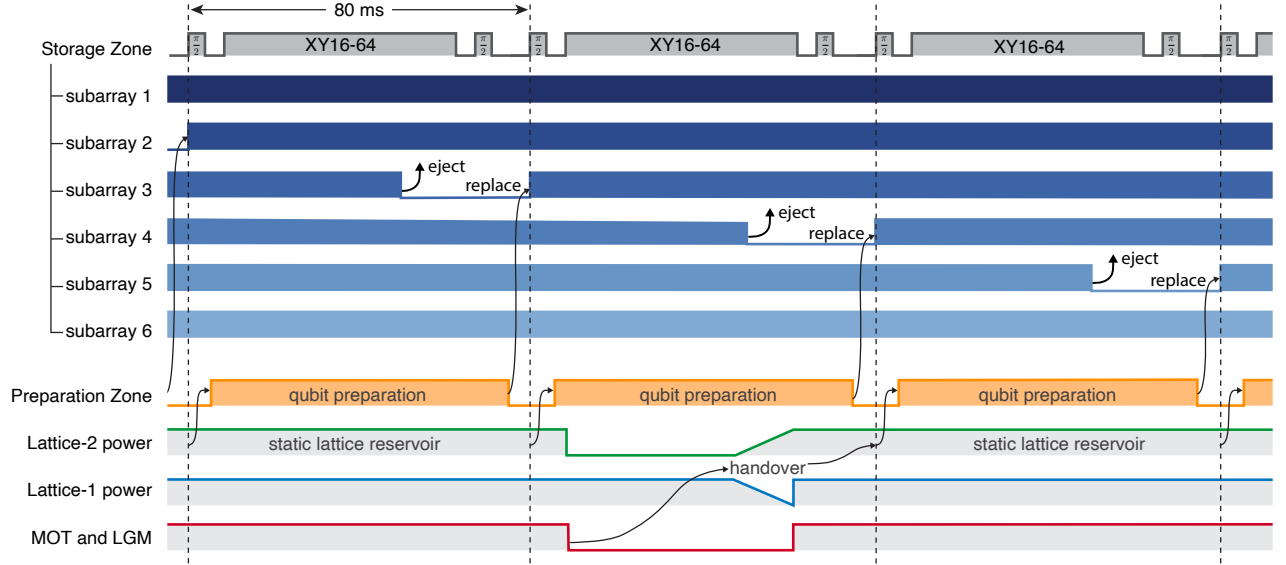
Extended Data Figure 6. **Preparation zone atom rearrangement and iterative assembly of the storage zone array.** **a**, Single-shot fluorescence images of the preparation zone atom array. Before rearrangement, atoms are stochastically loaded (top). After rearrangement, the target array is filled with near-unity probability (bottom). For this shot, the 600-site target array has zero defects. Explicitly ejecting atoms outside the target array is not necessary, as only the target array is picked up by AOD tweezers and transported to the storage zone. **b**, Preparation zone rearrangement histogram (500 trials) of 540 target sites. We achieve a 99.6% average filling fraction with 14% of the trials having zero defects. For visualization, trials with fewer than 530 atoms ($\approx 1\%$ of all trials) are grouped into the 530-atom bin. **c**, Storage zone loading histogram (300 trials). We achieve an average loading fraction of 98.5% (3,193 atoms). **d**, Storage zone iterative assembly scheme. In each iteration, 540 AOD tweezers pick up sorted atoms from the preparation zone target array (bottom), which are transported to the storage zone (top) to sequentially fill one of six subarrays (blue color shading). The AOD tweezers travel through wide channels in the storage array to avoid crosstalk with the static SLM tweezer traps. The schematic illustrates filling of the second subarray, where the first subarray has already been filled. See also Supplementary Movie.



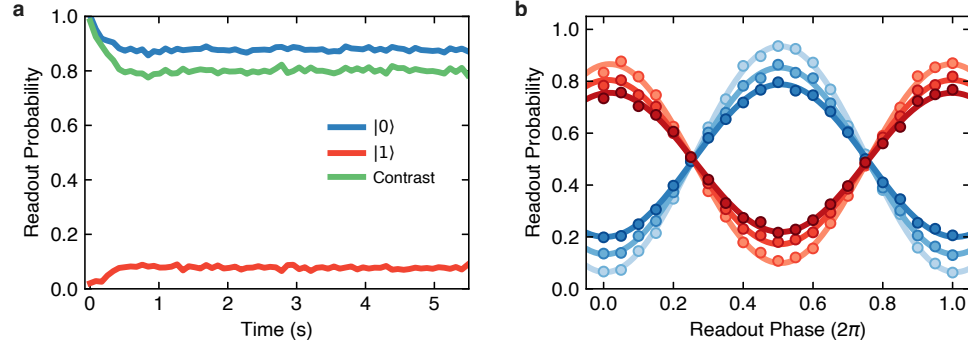
Extended Data Figure 7. **Raman and shielding beam characterization.** **a**, Rabi oscillations for each row of the storage qubit array. The variation of fitted Rabi frequency allows us to extract a Raman beam homogeneity of approximately 1.04% root-mean-square variation and 3.4% peak-to-peak variation on the atoms. **b**, Beam profile of the knife-edged flat-top 1529 nm shielding light, where the storage zone location is indicated. The plot on the right shows a zoomed-in line profile through the center of the beam, where the orange (gray) curve corresponds to the profile with (without) the knife edge. Evidently, cropping residual beam tails is imperative to avoid beam cross talk into the preparation zone (location marked with the black arrow).



Extended Data Figure 8. **Qubit depolarization under various conditions.** **a**, In main text Fig. 3b, we investigate how various parallel operations influence qubit polarization when initialized in state $|1\rangle$, where we expect a strong effect as pumping lights used for MOT and qubit preparation predominantly operate from $F = 2$. Here, we show a complementary analysis for qubits initialized in $|0\rangle$. Similarly comparing storage qubit depolarization during local qubit preparation with and without shielding, we are able to recover the measured T_1 -time up to the depolarization rate set by the lattice lights. As expected, we generally find lower depolarization rates compared to starting in $|1\rangle$. **b**, Summary of the fitted $1/e$ T_2 - and T_1 -times from Figs. 3a,b and ED Fig. 8a.



Extended Data Figure 9. **Experimental sequence for continuous reloading while maintaining qubit coherence.** Summary of the sequence used to achieve the results of Figs. 4b,c,d and ED Figs. 10a,b. In the storage zone, dynamical decoupling (except for Fig. 4b) and shielding are continuously applied to the storage qubits, while the respective oldest qubit subarray is discarded and refilled with fresh qubits from the reservoir. First, an initial $X_{\pi/2}$ pulse prepares qubits in a coherent superposition state. After XY16-64 decoupling, (remaining) coherence is briefly mapped back to population – typically into $|0\rangle$ with a $X_{-\pi/2}$ pulse – before the next qubit subarray is introduced. Thereby, qubits are in the equal superposition state for about 90% of total experiment duration. In ED Fig. 10b, we show an example of mapping back into alternating $|0\rangle$ and $|1\rangle$ populations by using a final $X_{+\pi/2}$ pulse instead. Throughout the experimental sequence, laser cooling in the MOT chamber, dual-lattice transport, and qubit preparation run in parallel in the background to provide a continuous supply of qubits. For Fig. 4b, no decoupling pulses are applied to the storage zone and we simply probe qubit depolarization under continuous reloading.



Extended Data Figure 10. **Coherence under continuous reloading.** **a**, Complementary analysis to Fig. 4c when array-averaging the probability to read out qubits in state $|0\rangle$ (blue) or $|1\rangle$ (red). The green line indicates the contrast, i.e. the difference of populations measured in $|0\rangle$ and $|1\rangle$. **b**, Similar to Fig. 4d, but instead with the decoupling sequence ($X_{\pi/2} - XY16-64 - X_{+\pi/2}$) applied during each reloading cycle. This results in alternating qubit states in the storage array (checkerboard pattern). The blue (red) curves represent the readout probability of even (odd) subarrays, indicated by the color shading.